ITERATIVE LEARNING CONTROL OF DIRECT WRITE ADDITIVE MANUFACTURING USING ONLINE PROCESS MONITORING

BY

CHRISTOPHER JOHN URBANSKI

THESIS

Submitted in partial fulfillment of the requirements
for the degree of Master of Science in Mechanical Engineering
in the Graduate College of the
University of Illinois Urbana-Champaign, 2023

Urbana, Illinois

Adviser:

Professor Andrew Alleyne

Abstract

The development of *in situ* process monitoring techniques for additive manufacturing (AM) has increased in recent years. While extrusion-based AM methods enable the fabrication of complex structures, ensuring the geometric accuracy of these structures requires direct measurements of the deposited material. Moreover, part fidelity can be improved by implementing control strategies to correct the geometric errors detected through process monitoring. Despite current research focusing on *in situ* process monitoring, few efforts investigate the relationships between process inputs and resulting print geometry for extrusion-based AM. Consequently, process control is often based on causal relationships or neglected altogether.

This work presents a process monitoring and control strategy for reducing the geometric errors in parts fabricated via extrusion-based direct write printing. A laser scanner integrated into the AM system directly measures the deposited material *in situ* during the print but not in real time. These measurements are processed online with a custom algorithm to determine the material's spatial placement and bead width errors. An iterative learning control (ILC) algorithm is applied to the deposition process to compensate for the geometric errors.

We experimentally validate the process monitoring and control strategy on a direct write printing system by fabricating 3D periodic lattice structures, specifically functionally graded scaffolds. Here, the ILC algorithm uses the online measurements to learn the errors in the structure's repetitive elements as they are printed, then corrects the errors in subsequently fabricated elements. The results show improved material bead widths in scaffolds fabricated using the proposed process monitoring and control strategy.

To Erica

Acknowledgments

First, I would like to thank my advisor, Dr. Andrew Alleyne, for all of his guidance, wisdom, and patience. His dedication to his students and their success is remarkable, which helps his students, including myself, reach their full potential. Dr. Alleyne has taught me invaluable lessons that I will carry with me throughout my career and life, and I am grateful to have had him as a mentor. This thesis would not have been possible without him.

As part of the Alleyne Research Group, I had the privilege to work alongside some of the brightest and kindest individuals I have ever met. The alumni, Spencer and Mindy, and senior members, Chris and Cary, shared their expertise, advice, and encouragement with me and helped foster a hardworking but fun environment. Additionally, my cohort—Frank, Dylan, Kurt, Phil, Kayla, and Reid—brought insights, enthusiasm, and humor that made my time and work much more enjoyable. These coworkers, who turned into friends, helped make my graduate experience incredibly memorable, and I feel so lucky to have met them.

I would also like to thank Jodi Gritten from the Center for Power Optimization of Electro-Thermal Systems (POETS), who made every day a happy one. My time in and out of the POETS office was always more fun because of her, and I appreciate all the care and support she shows for every student she works with.

I am forever grateful to my family, as I would not be where I am today without them. I am thankful for my parents, who have supported me with their unconditional love and provided countless opportunities to help me succeed. I am also thankful for my sister, Jenn, whose advice has guided me when I need it most, and for Robin, whose positivity and support

have always helped me through tough times.

Finally, I would like to thank my partner Erica for being the incredible person that she is and showing me never-ending love, encouragement, and patience. She always knows how to make me smile and never lets me lose sight of the important things in life, and for that, I am truly grateful.

Table of contents

Chapter 1

Introduction

The research presented in this thesis aims to improve the quality and reliability of direct write (DW) printing by reducing the geometric errors of fabricated structures. To achieve this, we develop a process monitoring system that directly measures the deposited material *in situ*, then processes the collected data online to determine the material's spatial and dimensional errors. The process monitoring system is paired with a learning controller to compensate for the measured errors. We implement the proposed process monitoring and control strategy on a DW printing system to fabricate multi-layer lattice scaffold structures. While this research targets DW printing of 3D periodic structures like lattice scaffolds, the generalized process monitoring and control approach can be extended to other extrusion-based additive manufacturing (AM) processes.

The remainder of this introduction provides background information pertinent to the topics covered in this thesis and is structured as follows: Section 1.1 presents an overview of DW printing, its use in fabricating 3D periodic structures like lattice scaffolds, and some of its limitations; Section 1.2 introduces the iterative learning control (ILC) algorithm used for process control and briefly reviews its usage in AM applications. Finally, an outline of the remaining chapters in this thesis is presented in Section 1.3.

1.1 Direct Write Printing

Direct write (DW) printing—also known as direct ink write, robocasting, or robotic deposition—is an extrusion-based AM technique. In DW, a continuous material filament is extruded from a nozzle and deposited layer-by-layer onto a surface, forming a 3D structure [1], [2]. The rheological properties of the materials used in DW, referred to as inks, are characteristic of yield-pseudoplastic fluids. As these inks are dispensed, they experience increased shear stresses when the material is forced through the nozzle, which causes the ink's viscosity to decrease, improving its flow. Once the ink exits the nozzle, the shear stresses are removed, so the material's viscosity increases, allowing the ink to retain its shape once deposited [2]–[5]. The variety of inks compatible with DW makes it a versatile AM technique with various applications, such as bioprinting.

1.1.1 Manufacturing of Lattice Scaffolds

One advantage of AM is its ability to fabricate complex structures that would otherwise be difficult to fabricate with other manufacturing methods [1], [6]. 3D periodic structures, such as the lattice structure shown in Fig. 1.1, are one example. In a lattice structure, rods are stacked atop one another to form a porous structure. Varying the width, spacing, or angle of these rods changes the macro porosity of the structure [1], which makes lattice-like structures useful in applications where controlling a structure's porosity is desirable.

The versatility of DW printing has enabled the fabrication of lattice structures for various applications. Lattices fabricated through DW methods have been used as scaffolds in tissue engineering [7]–[9], photonic band gap materials [10], [11], and drug delivery systems [12]. In these applications, the structure's porosity is integral to its function. Therefore, fabricating a structure with desired porosity characteristics via DW printing requires precise control over the spatial placement and size of the deposited lattice rods.

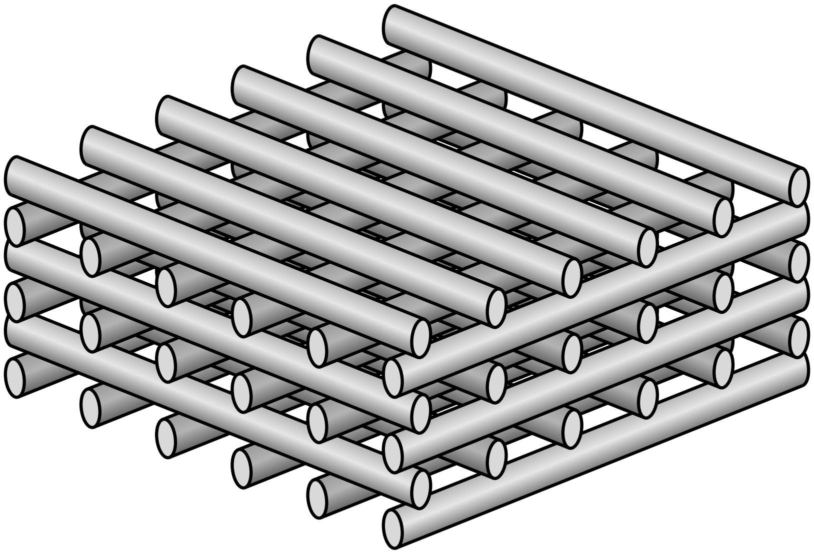

Figure 1.1: Example architecture for a lattice scaffold structure.

1.1.2 Current Limitations of Direct Write Printing

In DW printing, as with any extrusion-based AM technique, there are two main reference frames to consider (Fig. 1.2) [13]. Borrowing terms from robotics, we refer to the first reference frame as the *joint space* to represent the joint positions of the machine's axes. The second frame is the *task space*, which is the space where the machine's task is defined. In AM, the machine's task is material deposition, so the task space represents the material's spatial placement and dimensions. Although the structure's geometry is reflected in the task space, its reference trajectory is given in the joint space as the set of motions followed by the axes so that the nozzle traces the shape of the desired structure while depositing the material.

It is often assumed that accurate machine positioning in the joint space will translate to accurate material geometry in the task space. Previous work in DW has investigated using position feedback from encoders—which only provide information about the machine's position in the joint space—for precision motion control in the joint space [14]–[16]. However, nozzle alignment errors, nozzle tip deflection, and the nonlinear and time-dependent material behavior create a disconnect between the two spaces [13], [17]. As a result of the imperfect coordination between the two spaces, perfect tracking in the joint space is insufficient to

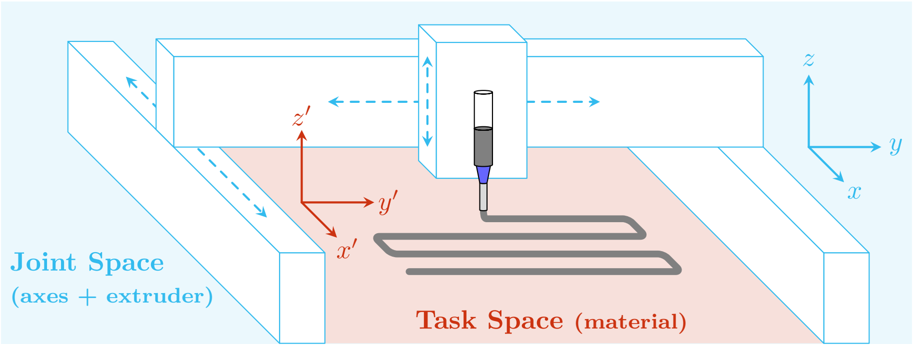

Figure 1.2: Visual representation of the two reference frames in AM. The joint space, depicted in blue, represents the joint positions of the machine's axes. The task space, depicted in red, represents the deposited material's geometry. Since the coordination between the two spaces is imperfect, perfect tracking in the joint space does not guarantee the desired material geometry in the task space. Adapted from [13].

guarantee that the material will be placed as desired in the task space, giving rise to geometric errors in the final structure. It follows that error detection using direct *in situ* process monitoring in the task space would enable correction of the material's spatial placement and dimensions, resulting in improved geometric fidelity of printed structures.

For extrusion-based AM processes like DW printing, current research efforts have mainly focused on *in situ* data collection [18], [19] while neglecting process control [20]. Furthermore, when process control is implemented, it is often based on causal relationships due to the limited investigation into the relationships between process inputs and print geometry for extrusion-based AM [18].

Although sparse, some efforts have been made in DW printing to incorporate process monitoring and control in the task space frame. Hoelzle *et al.* [21]–[23] monitored the deposition process with a vision system and used machine vision to calculate the material's volumetric flow rate. Likewise, Armstrong *et al.* [13], [24]–[26] determined the geometric errors from a 3D point cloud of the deposited material generated by moving a 2D laser scanner across the part. Both approaches effectively used iterative learning control algorithms to control the material geometry in the task space; however, the lack of online data processing meant information from the current print could not be used concurrently for control. In another approach, Piovarci *et al.* [27] trained a neural network in simulation to reduce under- and over-extrusion by modifying the print trajectory based on real-time feedback from a vision system. They demonstrated their process on outline and infill printing, but the limitations of their vision system restricted the approach to single-layer prints.

1.2 Iterative Learning Control

Iterative learning control (ILC) is a feedforward control strategy implemented on systems that perform the same task multiple times. First described in [28], the premise behind ILC is that system performance can be improved by learning from previous task iterations. By exploiting trajectory repetition, ILC is able to compensate for unmodeled dynamics, nonlinearities, and repeated disturbances [29]. For systems with a repeated reference trajectory, discontinuous operation, iteration-invariant dynamics, and iteration-invariant disturbances, ILC can achieve high-performance trajectory tracking without rigorous system modeling [30]–[33]. These conditions are common in manufacturing, making ILC well-suited for manufacturing applications.

ILC generates the feedforward control signals by storing the control inputs and errors of past iterations and mapping them to the current iteration control inputs. This process of updating the input signals occurs *offline* between iterations. ILC, therefore, is an appealing control strategy for systems that are difficult to measure *in situ* or in real time [21], [34]–[36] since offline measurements can be used to update the signals. Furthermore, while these systems often operate in open-loop, ILC can still be implemented if the system is open-loop stable [22].

Consider the discrete-time system P that maps the input signal $u_j(k)$ to the measured output signal $y_j(k)$. The error signal $e_j(k)$ is defined as the difference between the iteration-invariant desired reference trajectory $r(k)$ and the measured output for the current iteration

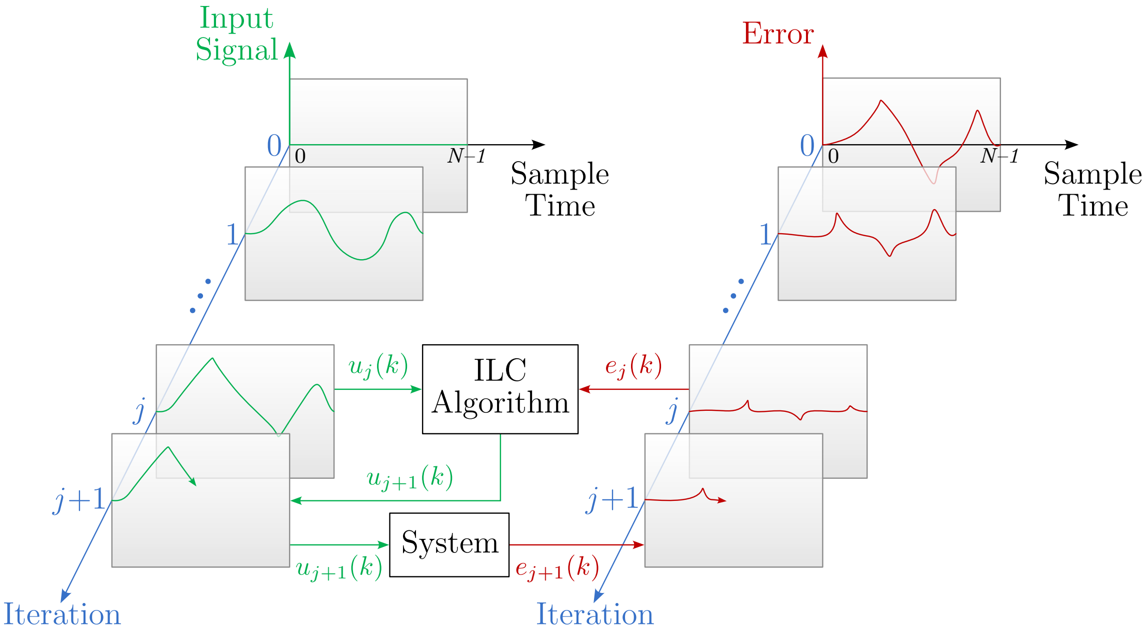

Figure 1.3: Visual depiction of the ILC algorithm illustrating the time and iteration domains. After each iteration, the previous input signal $u_j(k)$ and the resulting error signal $e_j(k)$ are used to calculate the updated input signal for the next iteration $u_{j+1}(k)$. Adapted from [29].

$y_j(k)$, given as

$$e_j(k) = r(k) - y_j(k) \tag{1.1}$$

where $k \in [0, N-1]$ is the discrete time index for the iteration with N samples, and the subscript j represents the iteration index. A commonly used ILC update law for calculating the next iteration's updated input signal $u_{j+1}(k)$ from the current iteration's error $e_j(k)$ and input $u_j(k)$ signals is

$$u_{j+1}(k) = Q(q)\left[u_j(k) + L(q)e_j(k)\right]. \tag{1.2}$$

Here q is the typical forward time-shift operator $qx(k) \triangleq x(k+1)$, while $Q(q)$ and $L(q)$ denote the Q-filter and learning function, respectively. Provided a properly designed Q-filter and learning function, the input signal converges to a final value with each subsequent iteration, consequently leading to the error signal converging to a small final value. Figure 1.3 visually depicts the ILC algorithm, illustrating the inputs to the update law and its iteration-to-iteration effect on the input and error signals. While Eq. (1.2) is the most commonly used update law, it should be noted that alternatives exist. Regardless, the premise of using previous input signals and resulting error signals to iteratively improve performance persists across update laws.

1.2.1 Iterative Learning Control in Additive Manufacturing

AM's repetitive processes and lack of online process monitoring tools make it well-suited for ILC. In addition to precision motion control [14]–[16], ILC has been utilized in DW printing to control the material's volumetric flow rate [21]–[23] and the filament's spatial placement and width [13], [24]–[26], as mentioned previously. Other applications of ILC to AM processes include controlling the melt pool temperature [37], [38] and layer height [38]–[41] in directed energy deposition, powder bed temperature distributions in laser powder bed fusion [42]–[44], and part size in fused deposition modeling [45]. Additionally, spatial ILC (SILC), which assumes a spatial relationship between inputs and outputs, has found use in material jetting for controlling droplet placement and size [46]–[49]. These implementations of ILC learn from previous parts or layers, except for [22], [23], which learn a set of basis signals that compose the complete trajectory. To our knowledge, learning within a layer has yet to be demonstrated, likely due in part to the absence and difficulties of online process monitoring in AM.

1.3 Thesis Organization

The remainder of this thesis is organized as follows: Chapter 2 describes the DW printing system and its positioning, deposition, and process monitoring subsystems used in this work; Chapter 3 introduces the methods utilized for process monitoring to position the sensor and process its output; Chapter 4 discusses the development of models relating deposition process inputs to print geometry and integrating these models with the measurements from the process monitoring system into an ILC algorithm to improve the material placement accuracy; Chapter 5 presents the fabrication of spatially graded scaffolds to demonstrate the proposed process monitoring and control strategy; Chapter 6 provides a summary of the research contributions and suggests directions for future work.

Chapter 2

Direct Write Printing System

Direct write (DW) printing is an extrusion-based AM technique in which a continuous material filament is extruded from a nozzle and deposited in layers to form a 3D structure. The two main components of a DW printing system are the positioning and deposition subsystems. The positioning system moves the deposition system through 3D space along a defined trajectory to deposit material in the shape of the desired part. The DW system used in this work also incorporates a process monitoring sensor that directly measures the deposited material *in situ*. This chapter describes the DW printing system and its components.

2.1 System Components

This section details the DW printing system's positioning system, end effector, deposition system, process monitoring sensor, and controller. An image of the printing system is shown in Fig. 2.1.

2.1.1 XYZθ Positioning System

A four-axis gantry (Aerotech AGS-10000) is used to control the position of the end effector on the DW system. The axes are stacked in a serial configuration, with the x-axis carrying the y-axis, the y-axis carrying the z-axis, and the z-axis carrying the θ-axis, as illustrated in Fig. 2.1. Brushless linear motors drive the x- and y-axes and rotary motors drive the z- and θ-axes. The z-axis motor connects to a precision ball screw via a belt drive, while the θ-axis motor connects to a harmonic drive. Each axis motor is a three-phase brushless DC motor connected to an amplifier (Aerotech BA Series) running in "current command." The current commands are sent to the amplifier by the Nservo controller as a ± 10 V analog output signal. Optical encoders provide position feedback for each axis at resolutions of 1 μm for the x- and y-axes, 0.1 μm for the z-axis, and 31.4 μrad for the θ-axis.

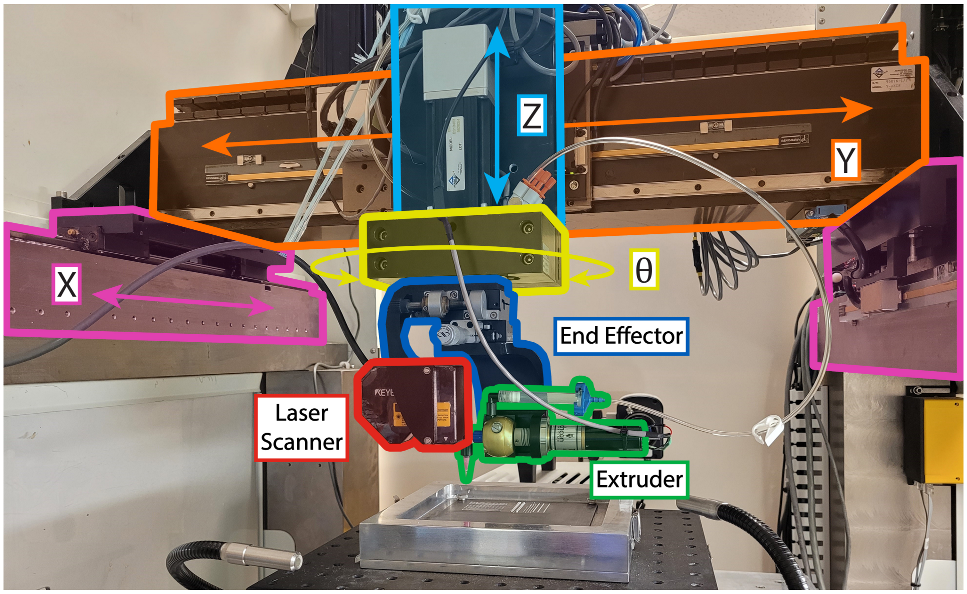

Figure 2.1: The DW printing system. An XYZθ positioning system moves the end effector containing the material deposition system (extruder) and process monitoring sensor (laser scanner) along a defined trajectory. As the end effector moves, the extruder deposits the material in the shape of the desired part, and the laser scanner measures the deposited material.

2.1.2 End Effector

The end effector attached to the θ-axis of the DW system contains the deposition system and process monitoring sensor, as shown in Fig. 2.2. The deposition system mounts to a two-axis fine linear positioning stage attached to the end effector. The fine positioning stages adjust the nozzle's position so that it is concentric with the axis of rotation of the θ-axis. The nozzle is aligned manually based on visual feedback from a camera fixed to the frame of the DW system. When the nozzle is concentric with the axis of rotation, moving the θ-axis does not change the position of the nozzle in the task space; thus, the position of the nozzle is controlled only by joint positions of the x-, y-, and z-axes.

An arm attached to the end effector positions the scanner so that the height of the nozzle is within the z-axis measurement range of the scanner, ensuring that the scanner can measure the deposited material. The arm also offsets the scanner from the nozzle and the axis of rotation of the θ-axis. Offsetting the scanner allows it to trail the nozzle during material deposition by rotating the θ-axis and end effector.

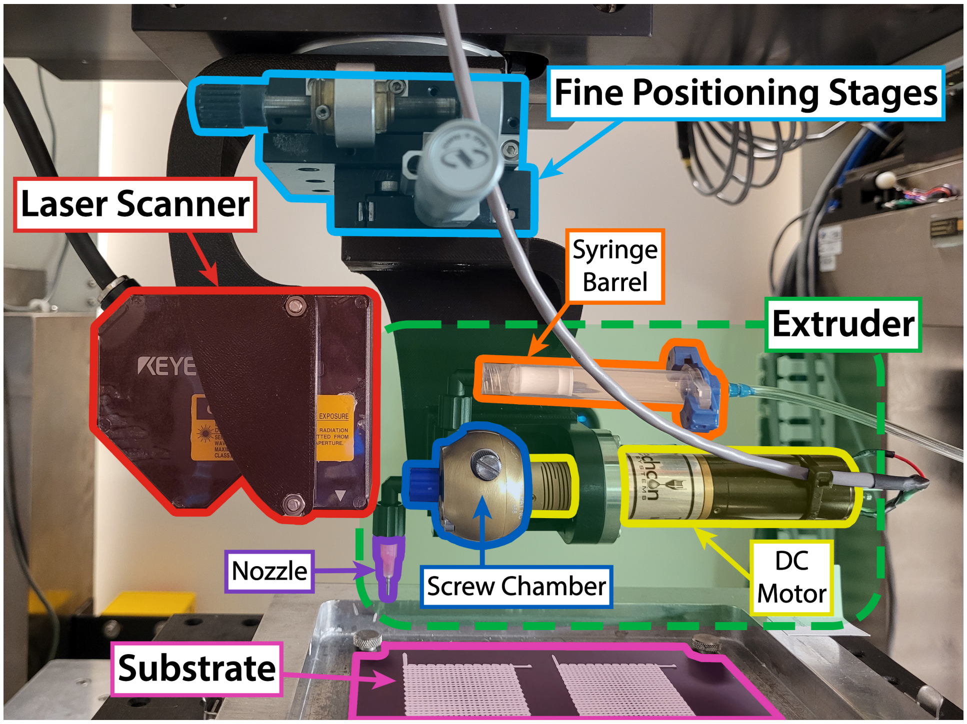

Figure 2.2: The end effector of the DW printing system. The end effector attached to the positioning system's θ-axis contains the process monitoring sensor (laser scanner) and the material deposition system (extruder). The fine positioning stages affix the extruder to the end effector and adjust the nozzle's position to align with the end effector's axis of rotation. As the nozzle traces out the shape of the desired part, the end effector is rotated so that the laser scanner tracks the deposited material.

2.1.3 Deposition System

The deposition system consists of both the ink material and the extrusion mechanism. This work uses Nivea Créme (Beiersdorf Global AG) as the ink for the deposition system because ink development is beyond the scope of this research; furthermore, Nivea Créme is commonly used as a test ink in bioprinting due to its consistent composition, low cost, and availability [50]. Using Nivea Créme avoids the need to fine-tune the ink's rheological properties to be suitable for printing and ensures consistent ink properties between prints. Further information regarding bioprinting inks can be found in [51]–[54].

The second component of the deposition system is the extrusion mechanism (green highlighted box in Fig. 2.2). Material is extruded by a motor-driven rotary screw (Techcon TS7000-DMP), also known as an auger. In the extrusion system, the material is stored in a syringe barrel (Nordson EFD) and supplied to the screw chamber by pressurized air (15 psi) acting on a piston. As the motor rotates the screw, the material is forced out of the chamber and through a deposition head. The DC motor driving the screw is connected to an amplifier (Advanced Motion Controls 12A8 servo drive) running in "current command." In this mode, the amplifier supplies a current to the motor proportional to a ± 10 V analog output signal generated by the controller. This mode is also called "torque command" since motor torque is proportional to the current supplied to the motor.

The deposition head consists of a Nordson EFD general purpose tip as the dispensing nozzle and is mounted perpendicular to the substrate onto which the material is deposited. Since the screw chamber is oriented horizontally relative to the substrate, it is connected to the nozzle via a 90° elbow.

2.1.4 Process Monitoring Sensor

The deposited material geometry is monitored in the task space using a 2D laser displacement sensor (Keyence LJ-G030), also known as a laser line scanner. Laser line scanners triangulate the displacement of an object by projecting a line of laser light onto the surface of an object and measuring the light reflection. The scanner triangulates the displacement at discrete points along the laser line, generating a 2D surface profile output as a vector of (x, z) coordinates relative to the scanner.

The LJ-G030 has a trapezoidal measurement region, and the profile measurements are given relative to its reference point 30 mm away from the bottom of the sensor (Fig. 2.3). In the z-direction, the measurement range for the scanner is ± 10 mm from the reference point. The sensor's x-direction measurement range depends on the position within the z-axis measurement range. Closer to the sensor, the x-direction measurement range is ± 10 mm from the reference point; further from the sensor, it is ± 12.5 mm from the reference point. The repeatability is 1 μm and 5 μm for measurements in the z and x-directions, respectively.

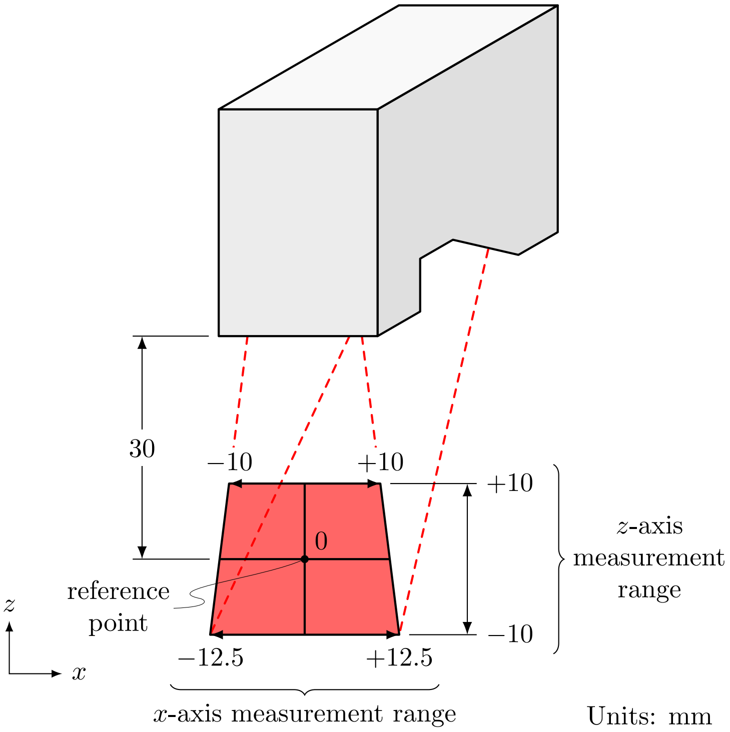

Figure 2.3: Measurement region of the Keyence LJ-G030 2D laser displacement sensor used for process monitoring.

During fabrication, a triggering signal is sent to the scanner by the controller. When triggered, the scanner records height measurements at fixed 33 μm intervals in the x-direction along the laser line. The height profile is then output as a proportional analog voltage signal at a fixed rate of 500 μs per measurement. This signal is sampled every 250 μs by a 16-bit analog input on the Nservo controller and discretized into a vector of (x, z) coordinates relative to the scanner. Once the profile signal is recorded, the controller sends another triggering signal to collect a new scan. Profiles are collected at an average rate of 1.77 Hz, with the limiting factor being the data collection rate of the Nservo controller since the scanner's profile output rate can reach up to 120 Hz.

2.1.5 Controller

An Aerotech Nservo controller generates the reference signals for the axes, extruder, and laser scanner; it also monitors the feedback signals for each axis and the analog output signal from the laser scanner. The Nservo controller runs the A3200 software motion controller (SMC), which interprets commands to generate the appropriate signals output by the Nservo controller. The A3200 SMC architecture is split into two levels that run independently. Time-critical activities such as the servo loops, motion profiles, and drive communication are handled at the lower level running on a real-time kernel; less time-critical activities, such as console displays and analog signal collection, are handled by the higher level running in Windows.

The A3200 SMC interprets commands written in the RS-274 numerical control language (G-code) in addition to other controller-specific commands. Using a C library for the A3200 SMC, a custom C++ program buffers commands into a queue on the A3200 SMC that the controller will sequentially execute. When consecutive motion commands are issued to the A3200 SMC, the interpolator blends the motions into a continuous motion trajectory. This means the axes do not decelerate between consecutive motions, which helps ensure the material deposition is smooth and consistent.

2.2 Coordinate Frames and Transformations

Since the components described in Section 2.1 are physically connected to the DW system, their positions relative to a coordinate frame can be described mathematically using transformations. Suppose point $\boldsymbol{q}$ has local coordinates $\boldsymbol{q}^A = \left[q_x^A,\, q_y^A,\, q_z^A\right]^\top$ with respect to frame A. The coordinates of $\boldsymbol{q}$ can be expressed relative to frame B using the equation

$$\bar{\boldsymbol{q}}^B = \mathbf{H}_A^B \bar{\boldsymbol{q}}^A \tag{2.1}$$

where $\bar{\boldsymbol{q}}$ is the homogeneous representation of point $\boldsymbol{q}$, given as

$$\bar{\boldsymbol{q}} = \begin{bmatrix} \boldsymbol{q} \\ 1 \end{bmatrix} \tag{2.2}$$

and $\mathbf{H}_A^B$ is the 4×4 matrix representing the coordinate transformation from frame A to frame B. These 4×4 homogeneous transformation matrices are constructed using matrices representing basic rotation and translation operations multiplied together. Translations along the x-, y-, and z-axes are respectively given by

$$\mathbf{T}_x(a) = \begin{bmatrix} 1 & 0 & 0 & a \\ 0 & 1 & 0 & 0 \\ 0 & 0 & 1 & 0 \\ 0 & 0 & 0 & 1 \end{bmatrix} \tag{2.3}$$

$$\mathbf{T}_y(b) = \begin{bmatrix} 1 & 0 & 0 & 0 \\ 0 & 1 & 0 & b \\ 0 & 0 & 1 & 0 \\ 0 & 0 & 0 & 1 \end{bmatrix} \tag{2.4}$$

$$\mathbf{T}_z(c) = \begin{bmatrix} 1 & 0 & 0 & 0 \\ 0 & 1 & 0 & 0 \\ 0 & 0 & 1 & c \\ 0 & 0 & 0 & 1 \end{bmatrix} \tag{2.5}$$

and the combined translation by the vector $\boldsymbol{v} = [a, b, c]^\top$ is given as

$$\begin{aligned} \mathbf{T}_{xyz}(\boldsymbol{v}) &= \mathbf{T}_x(a)\mathbf{T}_y(b)\mathbf{T}_z(c) \\ &= \begin{bmatrix} 1 & 0 & 0 & a \\ 0 & 1 & 0 & b \\ 0 & 0 & 1 & c \\ 0 & 0 & 0 & 1 \end{bmatrix}. \end{aligned} \tag{2.6}$$

Rotations about the x-, y-, and z-axes by the angles α, β, and γ are respectively given as

$$\mathbf{R}_x(\alpha) = \begin{bmatrix} 1 & 0 & 0 & 0 \\ 0 & \cos(\alpha) & -\sin(\alpha) & 0 \\ 0 & \sin(\alpha) & \cos(\alpha) & 0 \\ 0 & 0 & 0 & 1 \end{bmatrix} \tag{2.7}$$

$$\mathbf{R}_y(\beta) = \begin{bmatrix} \cos(\beta) & 0 & \sin(\beta) & 0 \\ 0 & 1 & 0 & 0 \\ -\sin(\beta) & 0 & \cos(\beta) & 0 \\ 0 & 0 & 0 & 1 \end{bmatrix} \tag{2.8}$$

$$\mathbf{R}_z(\gamma) = \begin{bmatrix} \cos(\gamma) & -\sin(\gamma) & 0 & 0 \\ \sin(\gamma) & \cos(\gamma) & 0 & 0 \\ 0 & 0 & 1 & 0 \\ 0 & 0 & 0 & 1 \end{bmatrix}. \tag{2.9}$$

2.2.1 System Coordinate Transformations

The coordinate frames of the DW system are illustrated in Fig. 2.4. The four frames, all of which follow the right-hand rule, are:

- Base Frame $O_B - x_B y_B z_B$: The frame fixed to the base of the gantry positioning system. The frame's axes align with the respective Cartesian axes of the DW system.
- End Effector Frame $O_E - x_E y_E z_E$: The frame attached to the end effector of the DW system. The z_E-axis points upward, parallel to the z_B-axis and aligned with the axis of rotation of the θ-axis. The x_E-axis points toward the nozzle frame.
- Nozzle Frame $O_N - x_N y_N z_N$: The frame with its origin O_N centered at the end of the nozzle. The z_N-axis points upward, parallel to the z_B-axis. The x_N-axis is parallel with the x_E-axis of the end effector frame and points in the same direction.
- Scanner Frame $O_S - x_S y_S z_S$: Profiles measurements from the laser scanner are given in coordinates relative to the Scanner Frame. The origin O_S is placed at the reference point, and the x_S- and z_S-axes align with the respective axes of the scanner shown in Fig. 2.3. The z_S-axis is parallel to the z_B-axis, and the x_S-axis is perpendicular to the x_E-axis.

The position of the axes relative to the base frame determines the position of the end effector frame. As the axes of the DW are stacked in a serial configuration, the position of the end effector frame is determined by a translation of each of the Cartesian axes, denoted by the vector $\boldsymbol{d}^{BE} = [X, Y, Z]^\top$, followed by a rotation about the current z-axis by the angle θ. Thus, the homogeneous transformation relating the end effector frame to the base frame is

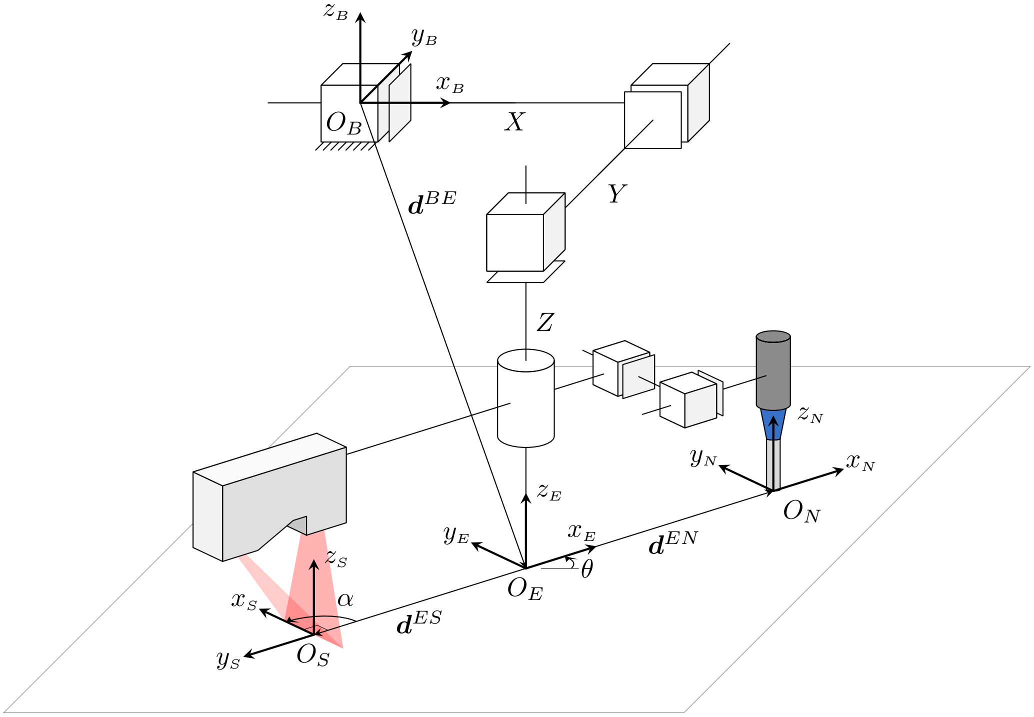

Figure 2.4: The coordinate frames of the DW system.

given by

$$\begin{aligned}\mathbf{H}_E^B &= \mathbf{T}_{xyz}\left(\boldsymbol{d}^{BE}\right)\mathbf{R}_z(\theta)\\ &= \begin{bmatrix}\cos(\theta) & -\sin(\theta) & 0 & X\\ \sin(\theta) & \cos(\theta) & 0 & Y\\ 0 & 0 & 1 & Z\\ 0 & 0 & 0 & 1\end{bmatrix}.\end{aligned} \tag{2.10}$$

Since the nozzle and scanner are attached to the end effector, the positions of the nozzle and scanner frames relative to the end effector frame are constant. These positions are represented by the vectors $\boldsymbol{d}^{EN}$ and $\boldsymbol{d}^{ES}$, which are the vectors from the end effector frame's origin O_E to the origins of the nozzle frame O_N and scanner frame O_S, respectively. Using Eq. (2.10), the coordinates of the nozzle can be expressed relative to the base frame as

$$\bar{\boldsymbol{d}}^{BN} = \mathbf{H}_E^B \bar{\boldsymbol{d}}^{EN}. \tag{2.11}$$

When the nozzle and the axis of rotation of the θ-axis are aligned, then $\boldsymbol{d}^{EN}$ is the zero vector, which substituted into Eq. (2.11) yields $\boldsymbol{d}^{BN} = \boldsymbol{d}^{BE}$. Thus, when the nozzle is aligned with the axis of rotation, its position coincides with end effector frame's origin and depends only on the translation of the Cartesian axes.

For the laser scanner, the homogeneous transformation relating the scanner frame to the end effector frame can be represented as a translation by the vector $\boldsymbol{d}^{ES} = \left[d_x^{ES}, d_y^{ES}, d_z^{ES}\right]^\top$, followed by a rotation about the current z-axis by the angle α, and is given by

$$\begin{aligned} \mathbf{H}_S^E &= \mathbf{T}_{xyz}\left(\boldsymbol{d}^{ES}\right)\mathbf{R}_z(\alpha) \\ &= \begin{bmatrix} \cos(\alpha) & -\sin(\alpha) & 0 & d_x^{ES} \\ \sin(\alpha) & \cos(\alpha) & 0 & d_y^{ES} \\ 0 & 0 & 1 & d_z^{ES} \\ 0 & 0 & 0 & 1 \end{bmatrix}. \end{aligned} \tag{2.12}$$

Multiplying Eq. (2.12) with the transformation $\mathbf{H}_E^B$ from Eq. (2.10) yields the transformation relating the scanner and base frames, given as

$$\begin{aligned} \mathbf{H}_S^B &= \mathbf{H}_E^B\mathbf{H}_S^E \\ &= \begin{bmatrix} \cos(\theta+\alpha) & -\sin(\theta+\alpha) & 0 & X + d_x^{ES}\cos(\theta) - d_y^{ES}\sin(\theta) \\ \sin(\theta+\alpha) & \cos(\theta+\alpha) & 0 & Y + d_x^{ES}\sin(\theta) + d_y^{ES}\cos(\theta) \\ 0 & 0 & 1 & Z + d_z^{ES} \\ 0 & 0 & 0 & 1 \end{bmatrix}. \end{aligned} \tag{2.13}$$

Since the x-axes of the scanner and end effector frames are perpendicular, $\alpha = \pi/2$, and

Eq. (2.13) further simplifies to

$$\mathbf{H}_S^B = \begin{bmatrix} -\sin(\theta) & -\cos(\theta) & 0 & X + d_x^{ES}\cos(\theta) - d_y^{ES}\sin(\theta) \\ \cos(\theta) & -\sin(\theta) & 0 & Y + d_x^{ES}\sin(\theta) + d_y^{ES}\cos(\theta) \\ 0 & 0 & 1 & Z + d_z^{ES} \\ 0 & 0 & 0 & 1 \end{bmatrix}. \tag{2.14}$$

2.3 Reference Trajectory

The reference trajectory input to fabricate a part is given as a deposition path and a width reference. The deposition path defines the Cartesian coordinates (x, y, z) that the nozzle must pass through to trace the desired shape of the part, while the width reference defines the width of the material filament along the deposition path. The trajectory is discretized into a set of N reference points uniformly spaced along the deposition path. At each reference point, the velocity and extrusion reference inputs are derived from the width reference based on mappings that are discussed in Chapter 4. The velocity and extrusion reference inputs are combined with the input deposition path to generate the motion and extrusion commands. These commands are issued to the A3200 SMC, generating the signals output by the Nservo controller to control the DW system.

Chapter 3

Task Space Process Monitoring

As discussed in Chapter 1, the improper coordination in AM between the joint and task spaces necessitates monitoring the material deposition process directly in the task space to determine the errors in the deposited material's geometry. In this chapter, we define the geometric errors related to the spatial placement and dimensions of the deposited material that the process monitoring system will measure. To determine the geometric errors, we use the 2D laser line scanner integrated into the DW system from Chapter 2 to take direct *in situ* measurements of the deposited material. A motion plan presented in this chapter enables the laser scanner to track and measure the material during printing. Computer vision techniques are used in a custom algorithm that processes these measurements into the material's geometric errors concurrently with the printing process.

3.1 Material Geometry Error Definitions

Accurate material geometry in AM is characterized by the spatial location of the extruded material relative to the desired position in the task space frame and the dimensions of the extruded material. For the lattice scaffolds fabricated in this work, the extruded material's dimension of interest is the width of the extruded material filament.

The spatial placement of the material is defined by how well the actual path of the deposited material tracks the desired path in the task space. Often in extrusion printing, it is assumed that accurate machine and extruder positioning in the joint space will result in accurate material geometry in the task space [13]. However, due to the imperfect coordination between the two spaces, perfect tracking in the joint space frame is insufficient to guarantee that the material will be placed in the task space at the desired location with the specified dimensions.

Material width is defined as the width of the deposited filament along the trajectory (Fig. 3.1a). Various factors can affect the material width, including changes in the axis speed, sharp corners in the reference trajectory, or clogs in the extrusion system. Axis speed is inversely related to the material filament width; given the same material flow rate from the extrusion system, a faster axis speed will reduce the material's width versus filaments extruded at a slower speed. Trajectories with tight corners can cause material buildup in these sections, leading to an increased width. Furthermore, clogs in the extrusion system reduce the material's flow rate, decreasing the filament width.

The process monitoring system developed in this work aims to directly measure the material geometry *in situ*, from which two error metrics related to the accuracy of the material deposition can be calculated. We will refer to these error metrics as the material's "geometric errors." The first metric is the material width error e_W, which is defined as the difference between the desired and actual widths of the material filament along the reference path (Fig. 3.1a). The second metric is the material centerline contour error e_c, which is defined as the distance from the reference path to the actual centerline of the material along the path normal vector $\boldsymbol{N}$ (Fig. 3.1b). The path normal vector is the vector in the xy-plane perpendicular to the path tangent vector $\boldsymbol{T}$ and points in the direction such that the two vectors $(\boldsymbol{T}, \boldsymbol{N})$ form a right-handed frame with the z-axis. The path tangent vector $\boldsymbol{T}$ is the vector in the xy-plane that is tangent to the centerline of the deposition path and points in the direction of motion along the path. The centerline contour error is positive or negative depending on whether the contour error points in the same or opposite direction of the path normal vector.

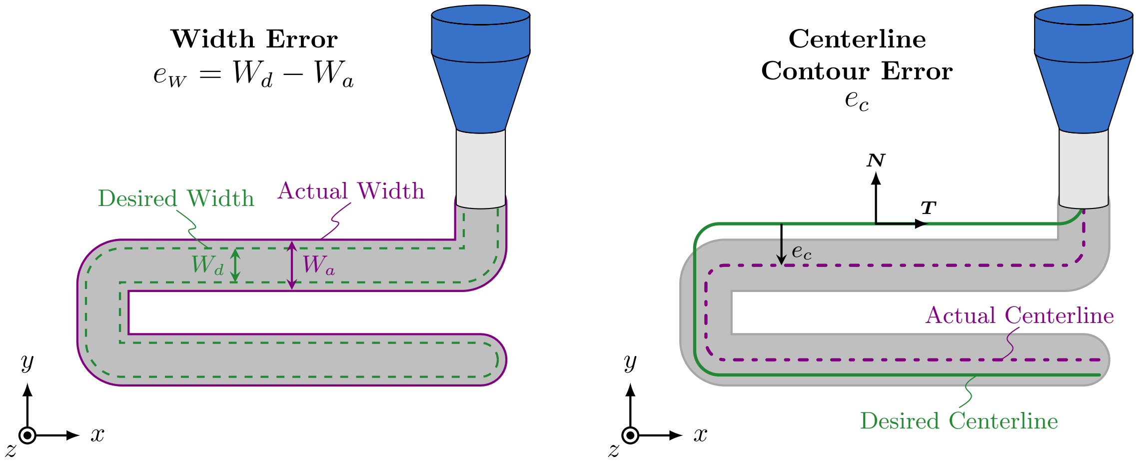

(a) (b)

Figure 3.1: Illustrations of the material width error (a) and the material centerline contour error (b). The depicted centerline contour error e_c is negative since it points in the opposite direction of the path normal vector $\boldsymbol{N}$. Adapted from [24].

3.2 Laser Scanner Motion Planning

When fabricating a part, the deposition path defines the set of Cartesian coordinates (x, y, z) that the nozzle must pass through to trace the shape of the desired part. The trajectory $\boldsymbol{p}(t)$ connecting these points can be represented by the path $\mathcal{P} = \left\{\boldsymbol{p}(t) \in \mathbb{R}^3 \,|\, t \in [t_i, t_f]\right\}$ parameterized by time t, where $\boldsymbol{p}(t_i)$ and $\boldsymbol{p}(t_f)$ are the initial and final points of the path, respectively. Since the nozzle is assumed to be aligned with the end effector's axis of rotation, the deposition trajectory also defines the trajectory for the end effector's position in the task space; this is equivalent to defining the trajectory of the Cartesian axes in the joint space.

Note that the deposition trajectory only specifies the position of the end effector, not its orientation, which is controlled by the rotational θ-axis. Since the laser scanner attached to the end effector is offset from the axis of rotation, its position is determined by the end effector's position and orientation. By defining the orientation of the end effector, we can rotate the laser scanner around the nozzle, enabling the laser scanner to track and take *in* *situ* measurements of the deposited material as the nozzle follows the deposition path. To determine the end effector orientation along the deposition path, thus the joint positions for the θ-axis, we define a motion plan for the laser scanner. We simplify the laser scanner's motion plan to two-dimensional motion in the xy-plane since rotating the θ-axis does not change the z-component of the laser scanner's position.

3.2.1 Motion Plan Objective

The purpose of the laser scanner is to take *in situ* measurements of the deposited material during the deposition process. Therefore, the laser scanner motion plan aims to center the laser scanner's measurement region over the reference material path while the nozzle follows the deposition path. This objective is chosen because the material must pass through the laser scanner's measurement region to be measured. To further simplify the motion planning, the deposition and material paths are assumed to be the same.

Although the reference material path will differ slightly from its actual path due to material placement errors, using the reference path for motion planning should not significantly impact the laser scanner's ability to take measurements of the material. As mentioned in Section 2.1.4, the laser scanner's measurement region extends a minimum of ± 10 mm from its center along its x-direction. This measurement region is much larger than the magnitude of the material placement errors, so material that deviates from the reference path should still pass through the measurement region and be measured.

3.2.2 Reference Path Construction

The position that centers the scanner's measurement region on the deposition path can be found by analyzing the workspace of the laser scanner. In robotics, the workspace is the locus of points that the origin of a frame can reach through all possible motions of the axes [55], [56]. While printing, the laser scanner's movement is restricted to the motion of the θ-axis since the deposition path dictates the motion of the Cartesian axes. Thus, the scanner's workspace is the circle traced out by the origin of the scanner frame $\boldsymbol{s} = [s_x, s_y]^\top$ if the θ-axis completed one full revolution (Fig. 3.2). This workspace also represents the locus of points that the center of the measurement region can reach. As the laser scanner's workspace changes based on the position of the nozzle, we denote the scanner's workspace at a given end effector position $\boldsymbol{p} = [p_x, p_y]^\top$ as $\mathcal{S}_{\boldsymbol{p}}$.

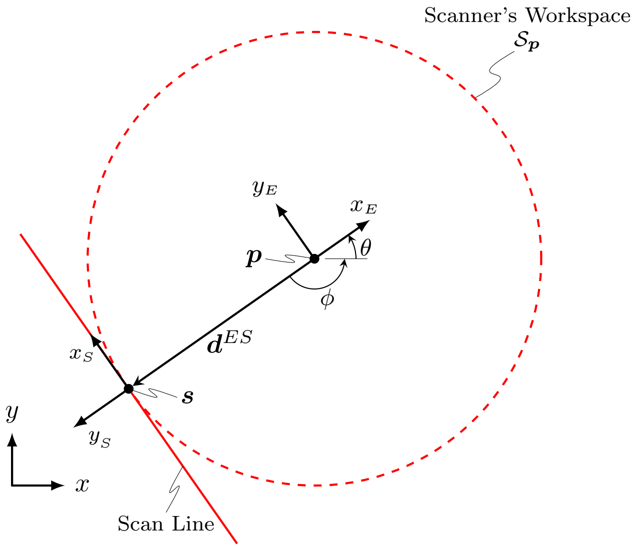

Figure 3.2: The scanner's workspace $\mathcal{S}_{\boldsymbol{p}}$, shown as the dashed red circle, represents the locus of points the scanner can reach when the end effector is at point $\boldsymbol{p}$. The scan line represents the projection of the laser scanner's measurement region in the xy-plane.

We define the set of points in the workspace $\mathcal{S}_{\boldsymbol{p}}$ using the forward kinematics of the scanner, which we derive from the homogeneous transformation for the laser scanner frame given by Eq. (2.14). Simplifying the kinematics to two dimensions, the coordinates of point $\boldsymbol{s} = [s_x, s_y]^\top$ in the workspace are given in terms of the θ-axis joint position θ and the nozzle position $\boldsymbol{p} = [p_x, p_y]^\top$ by the parametric equations:

$$s_x(\theta) = p_x + d_x^{ES}\cos(\theta) - d_y^{ES}\sin(\theta) \tag{3.1a}$$

$$s_y(\theta) = p_y + d_x^{ES}\sin(\theta) + d_y^{ES}\cos(\theta) \tag{3.1b}$$

where $\boldsymbol{d}^{ES} = \left[d_x^{ES}, d_y^{ES}\right]^\top$ is the constant vector from the end effector frame to the scanner frame. Alternatively, the workspace can be defined as the points on the circle centered at point $\boldsymbol{p}$ with radius $r_{\mathcal{S}}$, given as

$$(s_x - p_x)^2 + (s_y - p_y)^2 = r_{\mathcal{S}}. \tag{3.2}$$

Here, $r_{\mathcal{S}}$ is the length of $\boldsymbol{d}^{ES}$ projected onto the xy-plane, given as $r_{\mathcal{S}} = \sqrt{(d_x^{ES})^2 + (d_y^{ES})^2}$.

Since the scanner's workspace represents the locus of points reachable by the center of the measurement region, the position that centers the measurement region on the material lies at the intersection of the scanner's workspace $\mathcal{S}_{\boldsymbol{p}}$ and the deposition path $\mathcal{P}$. The intersection points can be found as the points of path $\mathcal{P}$ that satisfy Eq. (3.2) at the given nozzle position $\boldsymbol{p}$. However, the intersection between the workspace and deposition path is not always unique, as shown by the example in Fig. 3.3. Therefore, we define the desired position for the scanner $\boldsymbol{s}^d = \left[s_x^d, s_y^d\right]^\top$ as the intersection point that the nozzle has passed through most recently.

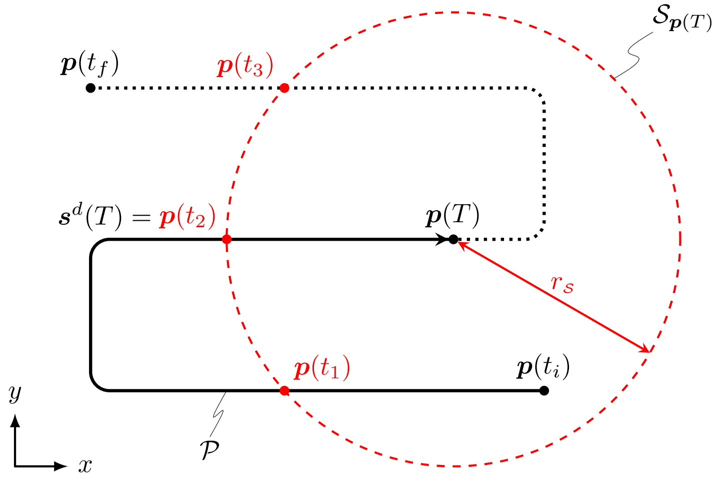

Figure 3.3: An example illustrating multiple intersections between the scanner workspace $\mathcal{S}_{\boldsymbol{p}(T)}$ and the deposition path $\mathcal{P}$. When the intersection point is not unique, the desired position for the scanner $\boldsymbol{s}^d$ is selected as the intersection point that the nozzle has passed through most recently. For this example, the desired scanner position is chosen as $\boldsymbol{s}^d = \boldsymbol{p}(t_2)$.

For example, let $\mathcal{P}$ be the deposition path defined on the interval $t \in [t_i, t_f]$, and $\boldsymbol{p}(T) \in \mathcal{P}$ be the position of the nozzle at time $T \in [t_i, t_f]$. Suppose the workspace at the position of the nozzle $\mathcal{S}_{\boldsymbol{p}(T)}$ intersects the path $\mathcal{P}$ at points $\boldsymbol{p}(t_1)$, $\boldsymbol{p}(t_2)$, and $\boldsymbol{p}(t_3)$, as shown in Fig. 3.3. When choosing the desired scanner position, we only select intersection points on the section of the path $\mathcal{P}$ the nozzle has traced out because those are the locations where material has been deposited. This section is the subset of $\mathcal{P}$ defined on the interval $t \in [t_i, T]$, which we denote as $\bar{\mathcal{P}}$. Since $\boldsymbol{p}(t_3) \notin \bar{\mathcal{P}}$, $\boldsymbol{p}(t_3)$ is not chosen as the desired position since the nozzle has not yet passed through that point. Conversely, $\boldsymbol{p}(t_1)$, $\boldsymbol{p}(t_2) \in \bar{\mathcal{P}}$, so the nozzle has passed through both points. However, the location of the nozzle $\boldsymbol{p}(T)$ is closer along the path to $\boldsymbol{p}(t_2)$ than to $\boldsymbol{p}(t_1)$. Therefore, $\boldsymbol{p}(t_2)$ is chosen as the desired position of the scanner $\boldsymbol{s}^d(T)$ when the nozzle is at point $\boldsymbol{p}(T)$.

Once the desired position for the scanner $\boldsymbol{s}^d = \left[s_x^d, s_y^d\right]^\top$ is found in the task space frame, the desired joint position for the θ-axis θ^d must be calculated. For a given position $\boldsymbol{p} = [p_x, p_y]^\top$ on the deposition path, the joint position θ that moves the scanner to point $\boldsymbol{s} = [s_x, s_y]^\top$ in the workspace can then be calculated using inverse kinematics. The inverse kinematics are derived geometrically from Fig. 3.2 as

$$\begin{aligned} \theta &= \phi + \pi \\ \theta &= \operatorname{atan2}(s_y - p_y, s_x - p_x) + \pi \end{aligned} \tag{3.3}$$

where $\operatorname{atan2}(y, x)$ is the two-argument arctangent function that returns a value ϕ on the interval $\phi \in (-\pi, \pi]$. Thus, Eq. (3.3) returns a value θ on the interval $\theta \in (0, 2\pi]$. Substituting $\boldsymbol{s} = \boldsymbol{s}^d$ into Eq. (3.3) yields the desired joint position θ^d for the θ-axis.

3.2.3 Feasible Trajectory with Constraints

To calculate the desired trajectory for the θ-axis using the methods described in Section 3.2.2, we first discretize the deposition trajectory $\boldsymbol{p}(t)$ into N points using a fixed sampling period T_s. The resulting discretized deposition trajectory $\boldsymbol{p}(k)$ defines the points $\boldsymbol{p}_k$ for $k = 0, 1, \ldots, N-1$ that the end effector must reach at times $t_k = kT_s$. For each point $\boldsymbol{p}_k$, the desired position of the scanner $\boldsymbol{s}_k^d$ is found and then converted into the desired joint position θ_k^d for the θ-axis. This results in a discretized trajectory $\theta^d(k)$ for the θ-axis synchronized with deposition trajectory $\boldsymbol{p}(k)$.

While the desired trajectory $\theta^d(k)$ satisfies the objective for taking *in situ* measurements, it assumes that there are no physical constraints for the θ-axis. Given that the axis will have limits on its position, velocity, and acceleration, it may be infeasible for the θ-axis to track the desired trajectory without exceeding those limits. Therefore, the optimal feasible trajectory $\theta^*(k)$ should minimize the deviation from the desired trajectory $\theta^d(k)$ to respect the path planning objectives while not violating the physical constraints imposed on the θ-axis. Written in mathematical terms, the optimal feasible trajectory $\theta(k) = \theta^*(k)$ solves the following constrained optimization problem:

$$\begin{aligned} \text{minimize} \quad & \frac{1}{2}\sum_{k=0}^{N-1}\left(\theta_k^d - \theta_k\right)^2 && \text{(3.4a)} \\ \text{subject to:} \quad & \theta^- < \theta_k \leq \theta^+ && \text{(3.4b)} \\ & \left|\dot{\theta}_k\right| \leq \omega_{\max} && \text{(3.4c)} \\ & \left|\ddot{\theta}_k\right| \leq \alpha_{\max}. && \text{(3.4d)} \end{aligned}$$

Here θ^+ and θ^- are the respective upper and lower position limits for the axis, and $\omega_{\max}$ and $\alpha_{\max}$ are the respective limits on the axis velocity and acceleration magnitudes. The discrete velocity and acceleration terms in Eqs. (3.4c) and (3.4d) are approximated using forward finite differences as

$$\dot{\theta}_k = \frac{\theta_k - \theta_{k-1}}{t_k - t_{k-1}} \quad \text{for} \quad k \in [1, N-1] \tag{3.5}$$

and

$$\ddot{\theta}_k = \frac{\dot{\theta}_k - \dot{\theta}_{k-1}}{t_k - t_{k-1}} \quad \text{for} \quad k \in [2, N-1] \tag{3.6}$$

respectively. We obtain the discrete trajectory $\theta^*(k)$ that solves the optimization problem given by Eq. (3.4) using the nonlinear programming solver `fmincon` in MATLAB.

3.3 Simulated Motion Plan

To assess the proposed motion planning scheme described in Section 3.2, we use a single-layer rectilinear raster pattern, shown in Fig. 3.4, as the deposition path. The raster path consists of four 34.5 mm long rods, each spaced 1.5 mm apart and connected with linear corner segments to form a continuous path. In the figure, the labels R_i and C_i denote the ith rod and corner segment, respectively. The rod segments' length is set greater than twice the offset distance between the scanner and nozzle $r_s = 15.25$ mm. This ensures that the scanner's workspace intersects the rod midpoints. Additionally, we extend the final segment with a lead-out line equal to r_s so that the final path points intersect the workspace after the nozzle has passed through them. The deposition trajectory follows the sample path at a constant axis velocity of $v = 1$ mm/s.

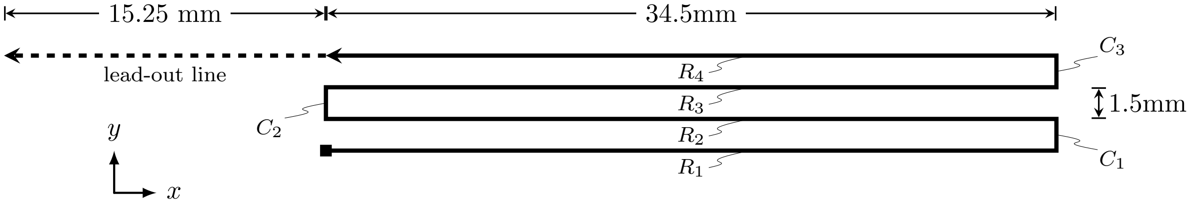

Figure 3.4: The deposition path used to assess the motion planning scheme for the laser scanner. The path segments are labeled R_i and C_i for the ith rod and corner segment, respectively. A lead out line, shown as the dashed line, is added to scan the final points of the path.

When calculating the desired trajectory for the laser scanner, the deposition trajectory is discretized with a sampling period of $T_s = 50$ ms. The feasible trajectory is generated from the desired trajectory using the constraints listed in Table 3.1.

Constraint	Limit
Lower Position θ^-	$-\frac{\pi}{6}$ rad
Upper Position θ^+	$\frac{7\pi}{6}$ rad
Velocity Magnitude $\omega_{\max}$	1.39 rad/s
Acceleration Magnitude $\alpha_{\max}$	3.49 rad/s^2

Table 3.1: Constraints for the θ-axis on the DW system.

The simulated position, velocity, and acceleration profiles for the desired reference trajectory $\theta^d(k)$ and the feasible trajectory $\theta^*(k)$ are shown in Fig. 3.5. The times when the nozzle reaches the end of a path segment are indicated with vertical dotted lines and labeled on the x-axis at the top of the figure; these labels correspond to the segments labeled on the deposition path in Fig. 3.4. Note that the desired trajectory $\theta^d(k)$ (solid black line) violates the velocity and acceleration constraints (dashed red line) in the rods R_2, R_3, and R_4 due to

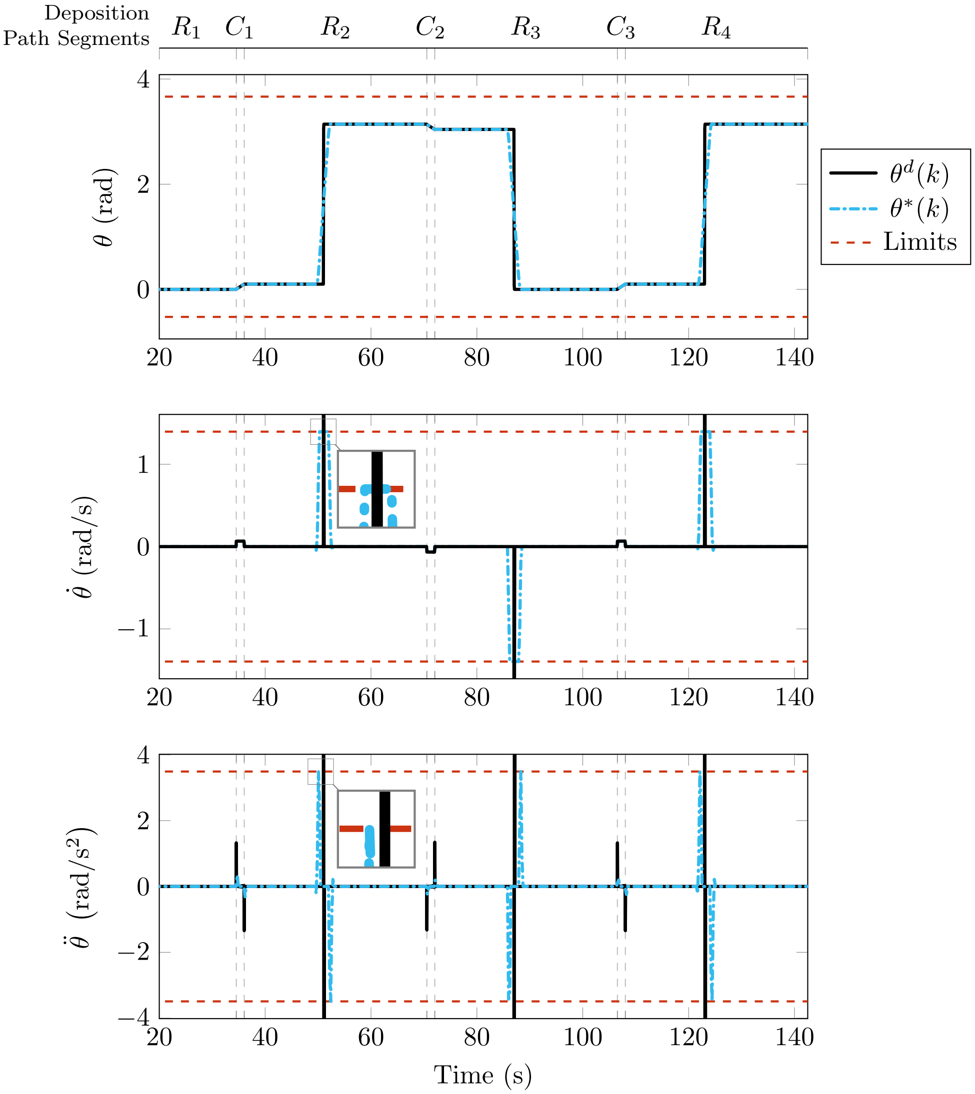

Figure 3.5: Position, velocity, and acceleration profiles for the desired and feasible trajectories of the θ-axis. The x-axis at the top indicates the segment of the deposition path that the nozzle is on at the given time, where the labels R_i and C_i correspond to the segments labeled in Fig. 3.4

the change in the desired position. In contrast, the feasible trajectory $\theta^*(k)$ (dashed blue line) starts the axis' motion in anticipation of the position change so that the axis' velocity and acceleration stay within the imposed limits during the move.

In addition to respecting the physical constraints of the axis, the feasible trajectory $\theta^*(k)$ should also position the laser scanner so it can take *in situ* measurements of the deposited material. The path traced out by the center point $\boldsymbol{s}$ of the measurement region only partially tracks the deposition path, as shown in Fig. 3.6. However, perfect tracking is not required for the entire deposition path to be scanned. If the deposited material enters the scanner's measurement region, it can be measured. For the laser scanner on the DW system, the measurement region extends a minimum of ± 10 mm from $\boldsymbol{s}$ along the scan line. Since the resulting area covered by the measurement region—shown in Fig. 3.6 as the region shaded in gray—completely encompasses the deposition path, the entire path can be measured.

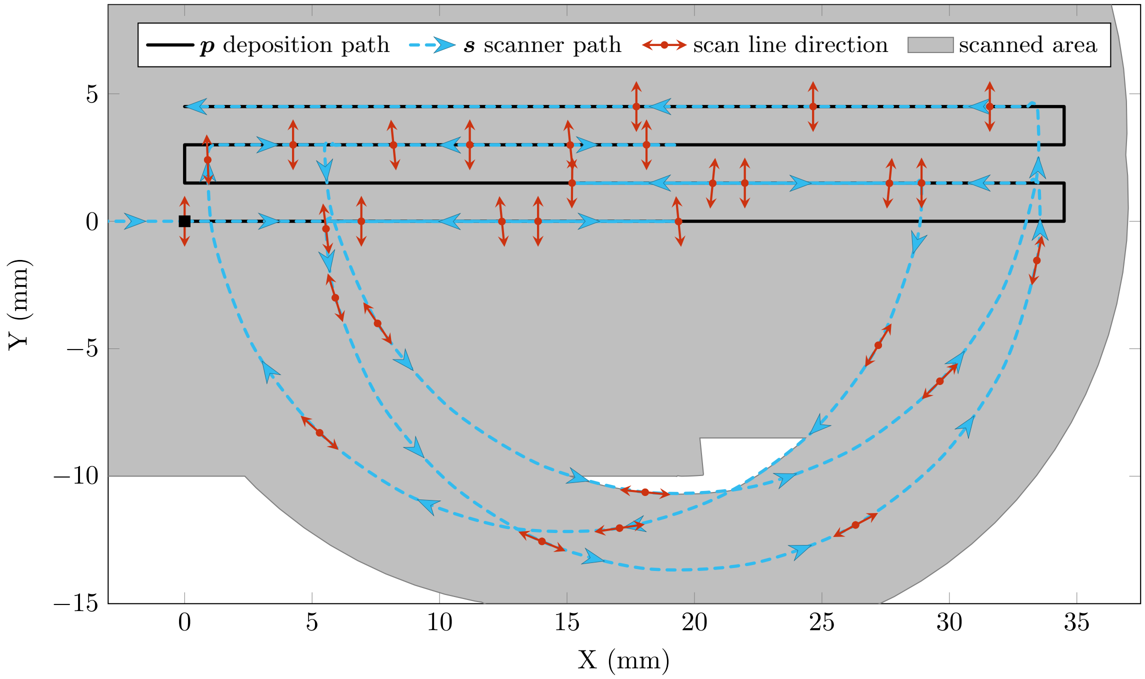

Figure 3.6: The path of the scanner and the resulting area scanned when tracking the feasible trajectory $\theta^*(k)$. The scanner's path is shown as the dashed blue line, and the blue arrowheads indicate the scanner's direction of motion. The orientation of the scan line is depicted at various points along the path by the red arrows. The area the laser scanner's measurement region covers (shaded gray region) completely encompasses the deposition path (solid black line), indicating that the entire deposition path can be measured.

While the area covered by the scanner's measurement region covers the entire deposition path, the scanner's sampling rate must also be considered to determine which points along the deposition path are scanned. Since the sampling rate is fixed, the density of points scanned will be inversely related to the scanner's linear velocity, which depends on both the deposition trajectory and θ-axis velocities. Accordingly, slower velocities are preferred when taking *in situ* measurements because that will increase the concentration of scanned points along the deposition path.

Figure 3.7 marks the approximate points on the deposition trajectory where profile measurements will be taken at the average scanner sampling rate. As mentioned in Section 2.1.4, the average sampling rate of the laser scanner is 1.77 Hz, meaning that a profile of the material is captured approximately every 0.56 seconds. When accounting for the sampling rate, the measured points are spaced an average of 0.56 mm along the rods, which is the approximate distance traveled by the Cartesian axes between scans at the given trajectory velocity of $v = 1$ mm/s. Conversely, no profile measurements are taken of the corner segments. Based on Fig. 3.6, the scanner rotates while its measurement region passes over the corner segments, which adds an additional component to the scanner's linear velocity. Given the short segment length, slow sampling rate, and θ-axis rotation increasing the scanner's velocity, the measurement region passes over the corner segments between profile measurements, resulting in their lack of measurements.

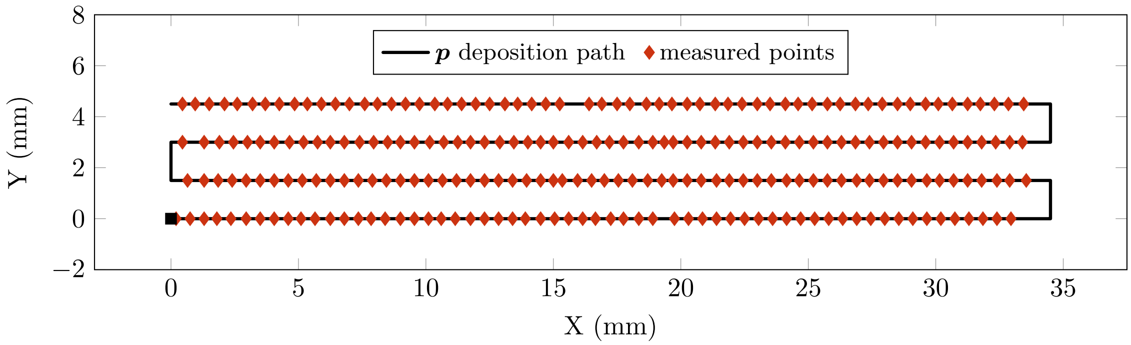

Figure 3.7: The approximate points on the deposition trajectory measured by the laser scanner at its average sampling rate.

It should be noted that the scanner's sampling rate can reach up to 120 Hz, but the hardware collecting the scanner's output signals limits it to 1.77 Hz. Therefore, hardware accommodating a faster sampling rate could be used to increase the measurement density in the corner segments. Additionally, measurement density would increase if the scanner's linear velocity were reduced during the rotation of the θ-axis. Achieving this would involve either limiting the θ-axis' angular velocity or shortening the offset distance between the scanner and nozzle r_S. However, both options have drawbacks; the former may reduce the tracking and scanning performance of the path plan, and the latter may not be possible due to physical interferences between components on the end effector.

3.4 Measurement Processing

The 2D laser line scanner incorporated into the DW system takes direct *in situ* measurements of the deposited material's surface profile. As the scanner moves over the deposited material, we process the surface profiles online to generate a 2D projection of the deposited material in the horizontal plane. This projection, which represents the material's geometry in the task space, is used to calculate the geometric errors.

The algorithm that generates the material's geometric errors is outlined in Fig. 3.8 and further described in Section 3.4.1. Visual depictions of the algorithm's steps are also shown in Fig. 3.9. We implement the algorithm in C++ utilizing OpenCV, an open-source computer vision library [57]. The developed program processes the profile measurements, generates the 2D projection of the deposited material, and extracts the material placement errors concurrently with the printing process.

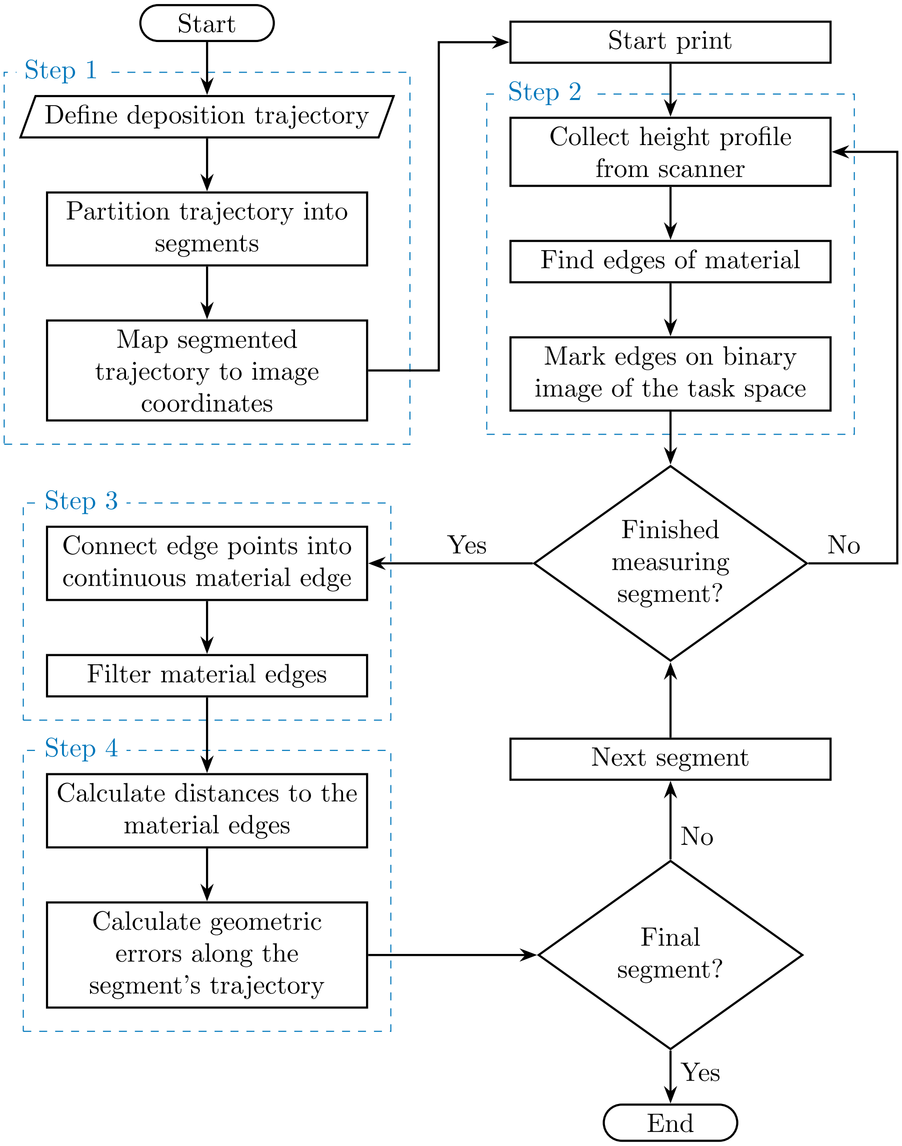

Figure 3.8: Flowchart of the measurement processing algorithm. The processes in the dashed boxes correspond to the steps described in Section 3.4.1.

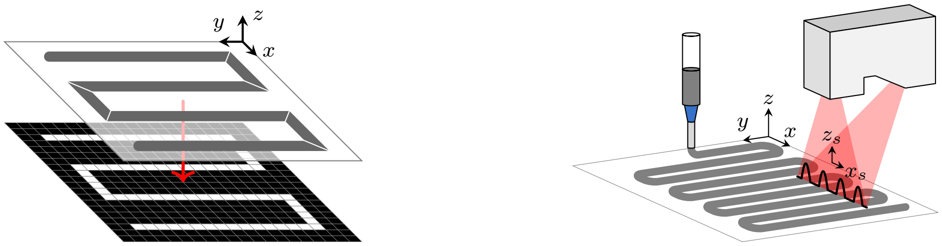

(a) Segment the deposition trajectory and map it to an image coordinate system.

(b) Measure height profiles *in situ*.

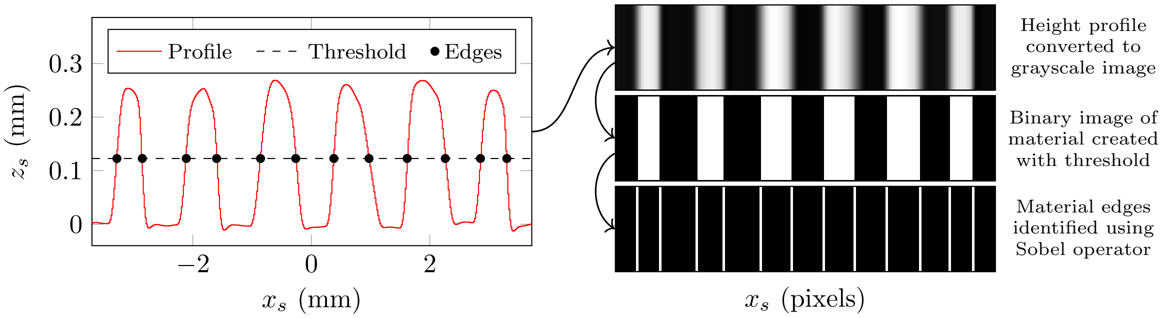

(c) Convert the height profile to a grayscale image, then threshold the profile to find the material edges.

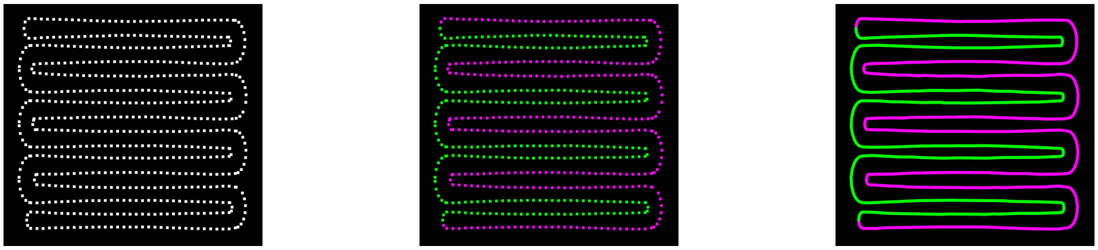

(d) Transform edge coordinates from the scanner frame to the task space frame and project them onto a binary image.

(e) Group the points into inner (green) and outer (magenta) edge points.

(f) Connect the inner and outer edge points to form a continuous material outline.

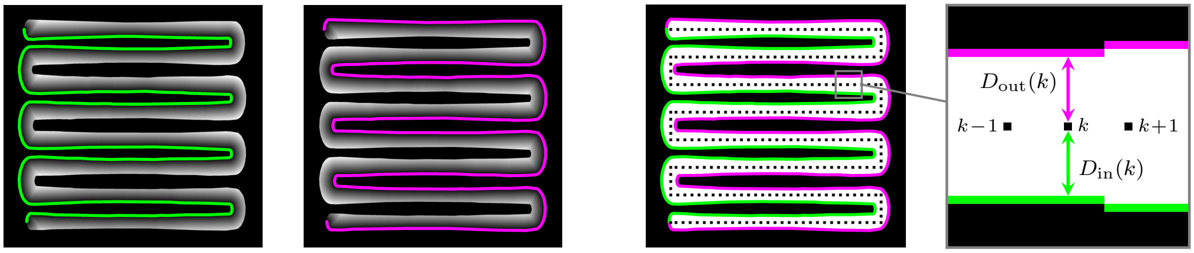

(g) Calculate the distance from the inner (green) and outer (magenta) edges using distance transforms.

(h) Use the distances from each edge to calculate the material width and centerline contour errors along the reference path.

Figure 3.9: Visual depictions of the main steps used to convert the profile measurements from the laser scanner into the material's geometric errors.

3.4.1 Measurement Processing Algorithm

Step 1: *Map the trajectory to an image*

Before the start of the print, the deposition trajectory is partitioned into smaller segments. Partitioning the trajectory enables the material's geometric errors to be determined before the print completes by measuring the material and processing the print segments in parallel. If the entire print trajectory is not partitioned, the projection and errors will only be calculated once the print finishes. For example, the sections processed for a raster pattern like the one shown in Fig. 3.9 correspond to the rod and corner segments of the pattern.

The 2D projection of each layer is represented as a separate binary image. For an individual layer, the coordinates in a region of interest surrounding the deposition path are mapped to the pixel coordinates of the image (Fig. 3.9a). A point with coordinates $\left(x^B, y^B\right)$ in the task space frame is related to the coordinates $\left(x^I, y^I\right)$ in the image coordinate system, given in pixels, using the following transformation:

$$\begin{bmatrix} x^I \\ y^I \\ 1 \end{bmatrix} = \mathbf{H}_B^I \begin{bmatrix} x^B \\ y^B \\ 1 \end{bmatrix}, \quad \text{where} \quad \mathbf{H}_B^I = \begin{bmatrix} 1/s_f & 0 & -x_0/s_f \\ 0 & 1/s_f & -y_0/s_f \\ 0 & 0 & 1 \end{bmatrix}. \tag{3.7}$$

The coordinates (x_0, y_0) define the origin of the region of interest in task space coordinates, and s_f is a scaling factor given in the length units of the task space per pixel. A scale factor of $s_f = 20$ μm/pixel is used in this work, meaning the center of each pixel in the image coordinate system represents the intersection point on a grid with a spacing of 20 μm in the task space.

Step 2: *Find the edges of the material in the surface profile*

When the scanner is triggered, the joint positions of each axis are stored, and the material surface is measured at n discrete points spaced at 33 μm intervals in the x-direction along the laser line (Fig. 3.9b). The measured height profile is output as a vector of z coordinates relative to the scanner coordinate frame. The height profile is converted into an $n \times 1$ 64-bit grayscale image, where the pixel's intensity value represents the height measurement at each x-coordinate along the laser line (Fig. 3.9c). Next, a binary image of the material is created by applying a threshold to the height profile such that points above the threshold indicate where the material was measured. The threshold value is obtained using the Otsu method, which is an algorithm commonly used in image processing for determining a threshold that separates pixels of foreground objects from background pixels in a grayscale image [58], [59]. When applied to the height profile, the threshold separates the deposited material from the background, creating a binary image of the deposited material. Taking the second derivative of the binary material profile using the Sobel operator [60], then finding the zero-crossings yields a binary image with the edge points of the material. The detected edge points given as x-coordinates in the scanner frame are then transformed to task space coordinates using the homogeneous transformation given by Eq. (2.14) and the stored axis positions. The edge points in task space coordinates are then projected onto a binary image using Eq. (3.7).

Step 3: *Determine the material outline from the measured points*

Once enough discrete edge measurements have been taken along a section of the material, the individual edge points can be connected to form a continuous material outline (Fig. 3.9f). Before the edge points are connected into a continuous edge, the points are first grouped into inner and outer edge points (Fig. 3.9e). We define the outer edge as the edge which the path normal $\boldsymbol{N}$ vector points toward and the inner edge as the edge which the path normal vector points away from, shown as the magenta and green edges in Fig. 3.10, respectively.

After separating the inner and outer edge points, outliers are removed from each group of points using a mask that approximates the shape of the edge. Any points outside the mask are treated as outliers and removed. Next, the remaining edge points are smoothed by attenuating the shorter wavelength components of the edge profile using a spatial Gaussian filter defined

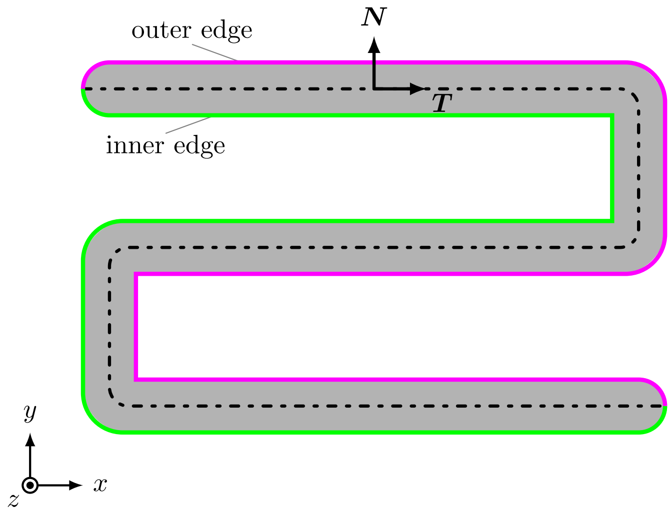

Figure 3.10: The path normal vector $\boldsymbol{N}$ points toward the outer edge, shown in magenta, and points away from the inner edge of the path, shown in green.

by its cut-off wavelength λ_c. Details regarding the implementation of the spatial Gaussian filter can be found in Appendix A. Finally, the smoothed points are connected to the nearest neighboring point using a piecewise linear curve to form the estimated continuous material edge (Fig. 3.9f). The outlier removal and smoothing processes are repeated independently for the inner and outer edge points, and the resulting edges are stored in separate binary images.

To create the mask applied to remove outliers, we first filter the edge points using a spatial Gaussian filter. This filter's cut-off wavelength is twice the cut-off of the filter that smooths the edge points once the outliers are removed (i.e., $\lambda_c^{\text{mask}} = 2\lambda_c^{\text{smooth}}$). The filtered points are then connected with a piecewise linear curve to create a masking edge. Finally, the masking edge is dilated using a square kernel as the structuring element to create the mask. The size of the morphology structuring element used to dilate the edge is chosen such that points greater than 0.26 mm from the approximated edge are removed as outliers.

It should be noted that the filter cut-off wavelengths and morphology structuring elements utilized in this step may need to be adjusted for other systems or applications. For instance, larger-scale AM systems may benefit from longer cut-off wavelengths and larger structuring elements since the parts fabricated on these system will likely have edge features with longer wavelengths. When tuning the parameters, longer cut-off wavelengths will attenuate shorter wavelength components of the profile, resulting in a smoother profile with less noise. However, if the cut-off wavelength is too long, the shorter details of the profile may be lost. Additionally, larger morphology structuring elements may introduce artificial features into the profile since fewer outliers will be removed. Therefore, choosing the filter and morphology parameters will depend on factors such as the length of an edge's designed features, the distance between sampled points, and the accuracy and precision of the edge point measurements.

Step 4: *Calculate the geometric errors*

The width and centerline contour errors are calculated by finding the distance from the reference trajectory to the inner and outer edges (Fig. 3.9h). Since the inner and outer edges are stored as binary images, the distance to the edges can be found using an image processing method known as a distance transform. In a binary image containing objects of interest, a distance transform maps the value of each pixel to the distance of the nearest object of interest [61], [62]. The mapped distances can be represented as an intensity value in a grayscale image, where brighter pixels represent longer distances, as illustrated by the example distance transform in Fig. 3.11. When a distance transform is applied to the binary image containing one of the material edges, a distance field is created where each pixel value is replaced with the shortest Euclidean distance to that material edge. The distance fields shown in Fig. 3.9g are masked to show only the distances inside the edges of the material as a grayscale intensity value.

By converting the points $\boldsymbol{p}(k)$ on the reference path to points $\boldsymbol{p}^I(k)$ in the image coordinate system using Eq. (3.7), the respective distance field can be sampled at those image coordinates to obtain the distances to the inner and outer edges from the reference path. These distances are shown in Fig. 3.9h as the green line labeled $D_{\text{in}}(k)$ and the magenta line labeled $D_{\text{out}}(k)$, respectively. As the distances obtained from the distance fields are given in units of pixels, the distances can be scaled from pixels to task space units by multiplying by scale factor s_f.

If the point $\boldsymbol{p}^I(k)$ lies within the boundary of the deposited material, the actual width of

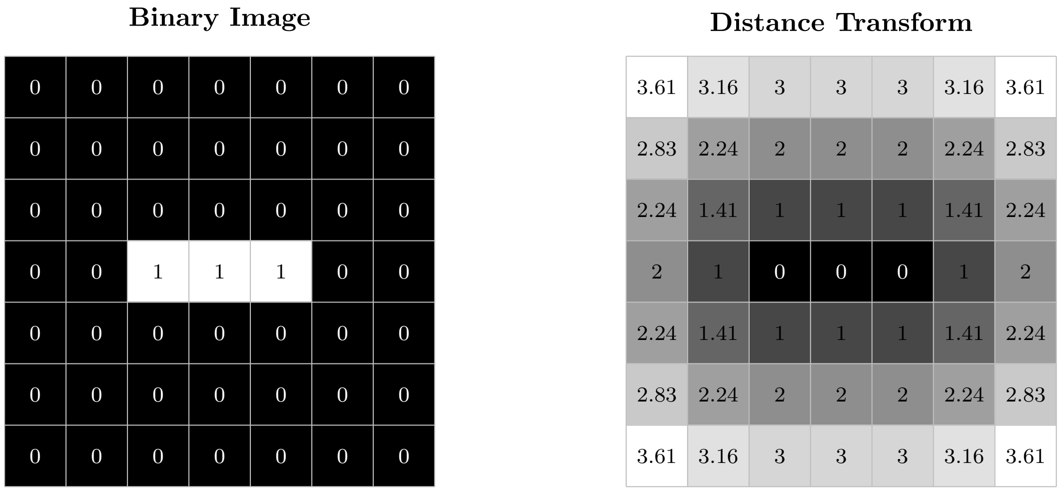

Binary Image

0	0	0	0	0	0	0
0	0	0	0	0	0	0
0	0	0	0	0	0	0
0	0	1	1	1	0	0
0	0	0	0	0	0	0
0	0	0	0	0	0	0
0	0	0	0	0	0	0

Distance Transform

3.61	3.16	3	3	3	3.16	3.61
2.83	2.24	2	2	2	2.24	2.83
2.24	1.41	1	1	1	1.41	2.24
2	1	0	0	0	1	2
2.24	1.41	1	1	1	1.41	2.24
2.83	2.24	2	2	2	2.24	2.83
3.61	3.16	3	3	3	3.16	3.61

Figure 3.11: An example of a distance transform. The binary image on the left indicates objects of interest as white pixels with a value of one. Using the distance transform, the image's pixel values are mapped to the distance of the nearest nearest non-zero pixel, creating the distance field on the right. When applied to a binary image of the material edge, the mapped values represent the distance in pixels to the material edge.

the material is the sum of the scaled distances to the inner and outer edges, i.e., $W(k) = s_f\big(D_{\text{out}}(k) + D_{\text{in}}(k)\big)$. The width error is then calculated as

$$e_W(k) = W_d(k) - s_f\left(D_{\text{out}}(k) + D_{\text{in}}(k)\right) \tag{3.8}$$

where $W_d(k)$ is the reference width at point $\boldsymbol{p}(k)$ on the reference path. Furthermore, the distance from either edge to the material's actual centerline will equal half the actual width $W(k)$. Recall that the centerline contour error e_c is defined as the distance from the reference path along the path normal vector to the actual centerline of the material. Since the contour error is positive or negative whether the contour error points in the same or opposite direction of the path normal vector, the contour error can be calculated by subtracting half the actual width from the distance to the outer edge. Thus, the centerline contour error is calculated as

$$\begin{aligned} e_c(k) &= s_f D_{\text{out}} - \frac{W(k)}{2} \\ &= s_f\,\frac{D_{\text{out}}(k) - D_{\text{in}}(k)}{2}. \end{aligned} \tag{3.9}$$

If the $\boldsymbol{p}^I(k)$ lies outside the boundary of the deposited material, Eqs. (3.8) and (3.9) no longer apply because the distances to the edges are scalar values. In this case, the actual width will be the magnitude of the difference between the edge distances, i.e., $W(k) = s_f \big| D_{\text{out}}(k) - D_{\text{in}}(k) \big|$. Thus, the width error is

$$e_W(k) = W_d(k) - s_f \left| D_{\text{out}}(k) - D_{\text{in}}(k) \right|. \tag{3.10}$$

Because $\boldsymbol{p}^I(k)$ is outside the boundary defined by the edges, the distance to the actual centerline will be half the width added to the distance to the nearest edge since the point. Therefore, the centerline contour error can be calculated as

$$e_c(k) = \begin{cases} -\left(\frac{1}{2} W(k) + D_{\text{out}}\right) & \text{if } D_{\text{out}} < D_{\text{in}} \\ \frac{1}{2} W(k) + D_{\text{in}} & \text{else} \end{cases} \tag{3.11}$$

which simplifies to

$$e_c(k) = \operatorname{sgn}(\Delta)\, s_f \, \frac{D_{\text{out}}(k) + D_{\text{in}}(k)}{2}, \quad \text{where } \Delta = D_{\text{out}}(k) - D_{\text{in}}(k). \tag{3.12}$$

Here, the sign function, denoted by $\operatorname{sgn}(\cdot)$, determines if the centerline contour error will be negative, which occurs when $D_{\text{out}} < D_{\text{in}}$.

Chapter 4

Control Strategy and Design

This chapter describes the methods to control the geometry of 3D periodic structures fabricated via direct write printing. Here, the focus is on controlling and reducing the errors in the material bead width along the deposition trajectory.

We first develop material models to predict the material's behavior during extrusion. These models are calibrated from experimental data, allowing us to map the material filament width to the input signals of the extrusion system. However, modeling the extrusion behavior is difficult and prone to errors due to the nonlinear and time-dependent flow behavior of the inks used in direct write printing [25], [63]. Therefore, relying solely on the material models to predict the final dimensions of the material can still result in geometric errors. To this end, we implement an iterative learning control (ILC) algorithm to correct dimensional errors obtained from the process monitoring system described in Chapters 2 and 3. By exploiting the repetitiveness of 3D periodic structures, the ILC algorithm learns the inputs for repetitive elements within the structure as they are fabricated. These learned inputs are then applied to fabricate the subsequent elements remaining in the structure.

4.1 Material Deposition Modeling

When fabricating a part, the width of the deposited material filament is specified at control points along the deposition path. For the rotary screw extrusion system described in Chapter 2, the input signals that can be modified to change the output filament width W are the extruder motor torque τ and the axis velocity v (Fig. 4.1). Other process parameters, such as the material, nozzle, and screw dimensions, can also affect the filament width; however, these parameters do not change during the deposition process. This section describes the development of the models that map the width reference signal to the extruder torque and axis velocity input signals.

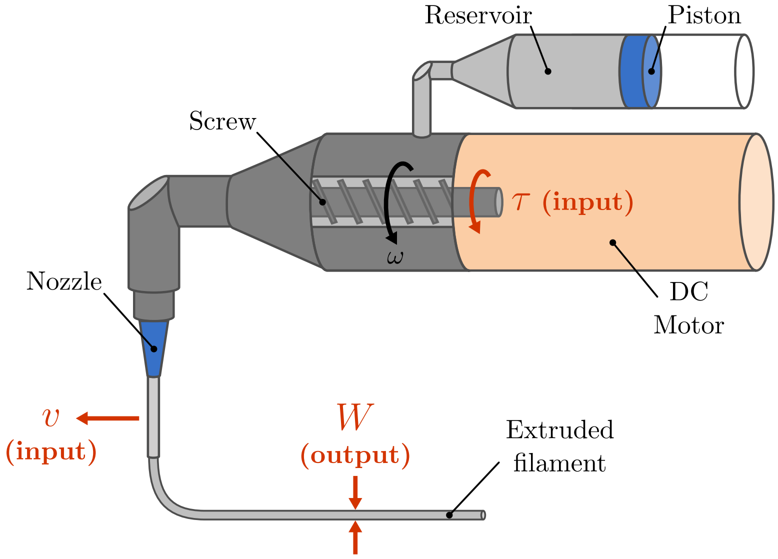

Figure 4.1: Schematic of the extrusion system. Pressurized air applied to the piston feeds material from the supply reservoir to the screw chamber. The screw rotates when the DC motor applies a torque τ (input) to it, forcing the material out through the nozzle. Moving the gantry axes at a velocity v (input) while extruding the material deposits a bead of material with a filament width W (output).

4.1.1 Model Development

Chen [64] developed a model for the flow rate from a motor-driven rotary screw through a nozzle, given as

$$Q + \left(\frac{c_{22}}{c_1^n} + \frac{c_{22}}{c_3^n} \right) Q^n = c_{21}\omega + c_{22} \left(P_p - P_a \right). \tag{4.1}$$

Here, the flow rate Q is expressed in terms of the power law index n, the rotational speed of the screw ω, the pressure applied to the material in the reservoir P_p, and the pressure at the nozzle outlet P_a. The coefficients c_1, c_{21}, c_{22}, and c_3 depend on the geometries of the screw, nozzle, and connection to the supply reservoir.

As the inks used in direct write printing are yield-pseudoplastic fluids, which by definition have non-Newtonian flow ($n \neq 1$), solving Eq. (4.1) is challenging since the equation is nonlinear. To facilitate the development of a simplified model, we assume the inks are Newtonian ($n = 1$); as a result, Eq. (4.1) has the following analytical solution for the flow rate:

$$Q = \frac{c_{21}\omega + c_{22} \left(P_p - P_a \right)}{1 + \frac{c_{22}}{c_1} + \frac{c_{22}}{c_3}}. \tag{4.2}$$

Although this assumption may reduce the models' accuracy over a range of operating conditions, the control strategy detailed later in this chapter will mitigate these errors introduced by the increased model uncertainty.

The flow rate can also be expressed as the product of the cross-sectional area of the material filament A_{cs} and the axis velocity v. Assuming the filament has a circular cross-sectional area, which is consistent with the observations in literature [2], [21], [25], [65], the flow rate is also given by

$$\begin{aligned} Q &= A_{cs} v \\ &= \frac{\pi}{4} W^2 v \end{aligned} \tag{4.3}$$

where W is the material width.

Combining Eqs. (4.2) and (4.3), then lumping the constant terms into the coefficient a_1

yields

$$W(\omega, v) = a_1 \sqrt{\frac{\omega + 1}{v}}. \tag{4.4}$$

While Eq. (4.4) expresses the material width W in terms of the axis velocity v input signal, it also depends on the screw speed ω, which is not an available input to the extrusion system.

When the extruder's DC motor applies a torque τ to the screw, it will accelerate until the screw reaches steady state, at which point its rotational speed will be constant. Here, a reasonable assumption is that the motor reaches equilibrium quickly. Since motor torque is proportional to screw speed at equilibrium, Eq. (4.4) can be approximated in terms of the input signals by substituting in torque for speed. Thus, Eq. (4.4) is approximated as

$$W(\tau, v) = a_1 \sqrt{\frac{\tau}{v}} \tag{4.5}$$

which expresses the material width W in terms of the axis velocity v and extruder torque τ input signals. If the axis velocity is held constant, the width becomes a function of the extruder torque, given as

$$W(\tau) = b_1 \sqrt{\tau}. \tag{4.6}$$

Similarly, if the extruder torque is held constant, the width becomes a function of the axis velocity, given as

$$W(v) = c_1 \sqrt{\frac{1}{v}}. \tag{4.7}$$

The coefficients for the models are determined by fitting the equations to experimental data collected from a series of calibration prints. When fitting the data, additional coefficients are added to Eqs. (4.6) and (4.7) to achieve a better fit. Therefore, the models fit to the experimental data are

$$W(\tau) = b_1 \sqrt{\tau} + b_2 \tag{4.8}$$

and

$$W(v) = c_1 \sqrt{\frac{1}{v}} + c_2. \tag{4.9}$$

4.1.2 Model Calibration

A series of calibration prints were fabricated to determine the coefficients of Eqs. (4.8) and (4.9). The prints consisted of a single layer of parallel rods, where each rod was extruded with the same axis velocity but a different extruder torque. After each rod, the torque input signal, which is proportional to the torque applied by the motor, was changed by 0.1 V over the entire 0.2–1 V range of inputs. The trajectory was repeated for velocities in the operating range of 1–3 mm/s at 0.5 mm/s intervals. This range was chosen as these speeds display consistent adhesion of the material filaments to the substrate. A Nordson 23GA general purpose tip with an inner diameter of $\varnothing = 330\ \mu\text{m}$ was used for the nozzle of the extrusion system. The nozzle was offset above the substrate by a layer height of $0.75(\varnothing)$, where $\varnothing$ is the nozzle's inside diameter. An example calibration print is shown in Fig. 4.2.

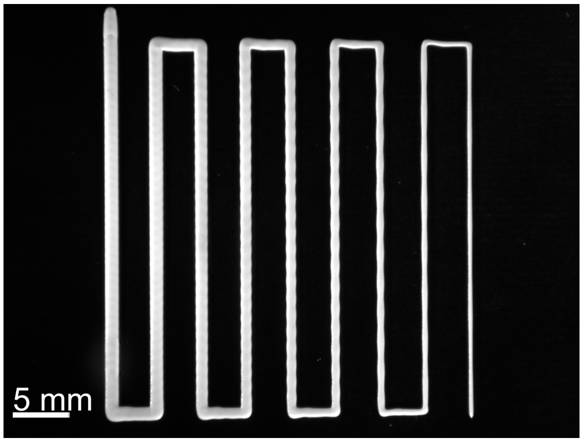

Figure 4.2: Example calibration print used to identify the coefficients of the material models. The material was extruded at a constant axis velocity while the extruder torque was changed after each vertical rod. The print was fabricated as a continuous extrusion, resulting in short segments of material connecting the ends of the rods. However, the width of these connecting segments was not used when calibrating the material models.

The material width along the rods was computed from profile scans collected by the Keyence laser scanner using the process described in Section 3.4. An average width was calculated for each rod, and Eqs. (4.8) and (4.9) were fit to the experimental data, as shown in Fig. 4.3. The resulting coefficients for Eqs. (4.8) and (4.9) are listed in Tables 4.1 and 4.2, respectively.

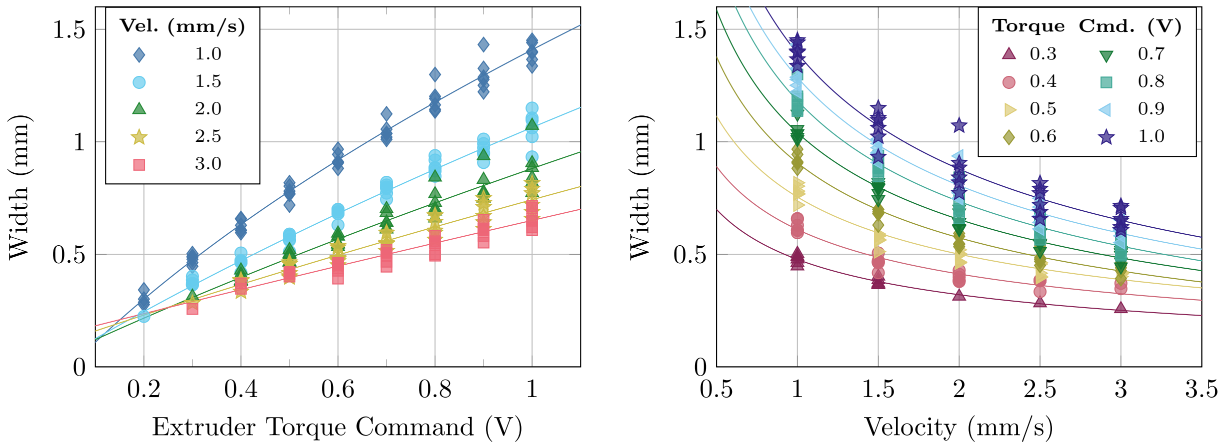

Figure 4.3: The experimental data from the calibration prints with the curve fits used to determine the coefficients of the models (Eqs. (4.8) and (4.9)) relating the output material width to the torque (left) and velocity (right) inputs.

v (mm/s)	b_1	b_2
1.0	2.03	-0.64
1.5	1.55	-0.50
2.0	1.31	-0.44
2.5	1.02	-0.28
3.0	0.83	-0.19

Table 4.1: Coefficients of Eq. (4.8) for different constant velocity inputs.

τ (V)	c_1	c_2
0.3	0.54	-0.06
0.4	0.68	-0.07
0.5	0.87	-0.11
0.6	1.14	-0.23
0.7	1.32	-0.28
0.8	1.53	-0.35
0.9	1.64	-0.35
1.0	1.76	-0.36

Table 4.2: Coefficients of Eq. (4.9) for different constant torque input commands.

4.2 Iterative Learning Control

Modeling the material extrusion dynamics is complex due to the material's nonlinear and time-dependent flow behavior. While the material models developed in Section 4.1 allow us to map material widths to the extruder torque and axis velocity input signals, relying solely on the models may still result in fabricated parts with geometric errors due to the simplifications and uncertainties of the model. The inability to accurately predict the material behavior using the models warrants the use of process monitoring and control strategies to enable the measurement and correction of dimensional errors.

The process monitoring system described in Chapters 2 and 3 directly measures the deposited material *in situ*. As discussed in Section 3.4, these measurements are processed online, determining the material's geometric errors in a segmented fashion. Since these errors are not obtained in real time, ILC is an appealing control strategy because it updates the input signal offline between iterations of the given task. Moreover, ILC is well-suited for AM since AM processes often include trajectory repetition—for example, repeating the same deposition trajectory between parts or layers.

As this work focuses on the fabrication of lattice scaffolds, we leverage the repetitiveness of 3D periodic structures to decompose the structure into sets of repeating elements. Rather than treating each structure as a single task, the repeated elements can be treated as repeated sub-tasks that are learned individually using ILC. The concatenation of these sub-tasks forms the sequence of operations that fabricate the desired structure. When combined with the online measurements from the process monitoring system, this segmented ILC approach is used to correct dimensional errors online without the need to suspend the print process.

4.2.1 Trajectory Partitioning

ILC typically tracks a repeated reference trajectory on systems with discontinuous operation, iteration-invariant dynamics, and iteration-invariant initial conditions. When applying

ILC to learn the sub-tasks instead of the complete trajectory, these characteristics influence the choice of sub-tasks that partition the trajectory. Accordingly, the sub-tasks are chosen with the following properties:

1. *Repetitive within the main task*—A sub-task should repeat within the main task to provide the trajectory repetition necessary for ILC to learn the given sub-task.
2. *Spatially-invariant dynamics*—Analogous to the iteration-invariant dynamics typically required for ILC, spatially-invariant dynamics allow the repetitive sub-task trajectories to be rotated and translated in space without their dynamics changing.
3. *ILC update interval*—Typically, ILC uses a task's discontinuous operation to update the input signals offline between iterations. With the segmented ILC approach, the sub-task sequence should have periods between sub-task iterations during which the ILC updates can occur. This allows the ILC algorithm to run and update signals without suspending the main task, ensuring its operation remains continuous.

While these properties guide the selection of sub-tasks, the final choice will be trajectory and system dependent.

The use of time-delayed measurements also influences the sub-task selection. When the measurements are time-delayed, the time interval between sub-task iterations must be longer than the combined measurement delay and time to perform the ILC updates. Otherwise, the next iteration of the sub-task will start before the ILC algorithm can update the input signals from the previous iteration.

4.2.2 Partitioning the Scaffold Trajectory

3D periodic structures, like the lattice scaffolds focused on in this work, are constructed of elements that repeat within the structure. When fabricating a multi-layer lattice scaffold, we use a deposition trajectory like the one shown in Fig. 4.4, where the trajectory for each layer follows the same rectilinear raster pattern that is rotated 90° relative to the previous layer. Since each layer's trajectory is the same, we define the following three sub-tasks to partition a single-layer raster trajectory: *odd-numbered rods*, *even-numbered rods*, and *corners*. These sub-tasks are illustrated in Fig. 4.5, which colors the trajectory based on the segment's respective sub-task.

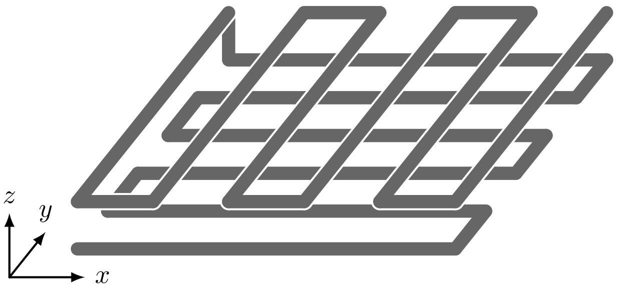

Figure 4.4: Deposition trajectory for a lattice scaffold structure. Each layer of the structure has a trajectory that follows a rectilinear raster pattern.

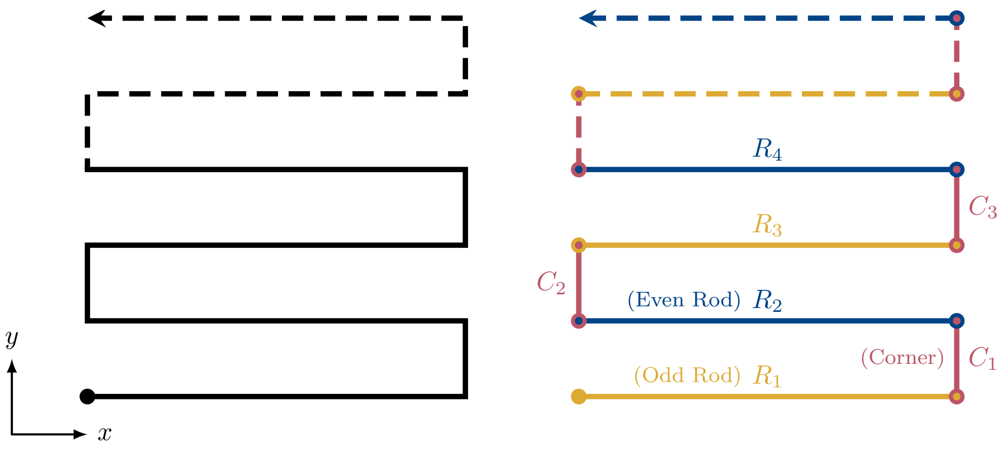

Figure 4.5: The trajectory for a single layer of a scaffold structure (left) is partitioned using repeating elements as the sub-tasks (right). The red, blue, and yellow segments of the partitioned trajectory correspond to the odd-numbered rod, even-numbered rod, or corner sub-tasks.

A diagram of the sub-task sequence with the measurement and ILC update intervals for the chosen sub-tasks is shown in Fig. 4.6. While this partitioning of a lattice scaffold is not unique, the selected sub-tasks provide sufficient time between sub-task iterations to acquire the measurements and update the input for the next iteration, as depicted in the figure. Other choices of sub-tasks, such as treating all rods as a single sub-task, may not provide sufficient time for the process monitoring system to finish measuring the sub-task before its next iteration.

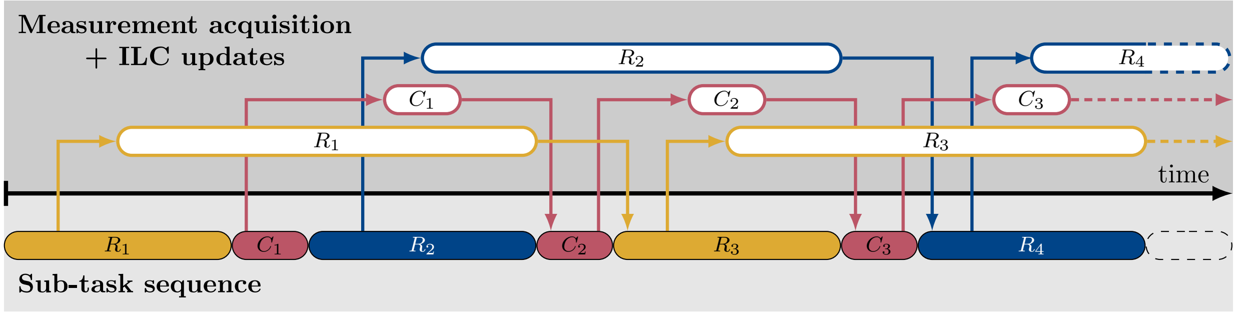

Figure 4.6: The sub-task sequence for the raster trajectory from Fig. 4.5 is depicted as the filled segments in the light gray region. The intervals during which a sub-task's measurements and ILC updates occur—depicted as the outlined segments in the dark gray region—must complete before the next iteration begins. The arrows indicate the flow of information from the previous sub-task to the process monitoring system and ILC algorithm, then to the next iteration. As the sub-tasks execute, their errors are measured and then used by the ILC algorithm to update the inputs for the next iteration.

4.2.3 Iterative Learning Controllers

For each sub-task, ILC is used to modify the width reference signal before it is mapped to the extruder inputs using the models developed in Section 4.1. The ILC update law used to determine the input for the subsequent iteration is

$$u_{j+1}^m(k) = u_j^m(k) + Q^m(q)\left[K_p^m e_j^m(k)\right] \tag{4.10}$$

which uses a proportional, or P-type, learning function. Here, the superscript m indicates the sub-task index, and K_p^m is the proportional gain. Although the update laws for each sub-task are separate, all update laws use a learning function with the proportional gain of $K_p = 1$ and the same Q-filter $Q(q)$. Including a Q-filter in Eq. (4.10) can help improve the error convergence by filtering out high-frequency noise [29]. In this work, the Gaussian filter described in Section 3.4.1 that smooths the measured material edges acts like a lowpass Q-filter applied to the error signal. Alternatively, using an error estimate in Eq. (4.10) may achieve similar improvements to the error convergence as a substitute for the more conventional Q-filter.

Chapter 5

Experimental Validation

This chapter discusses the fabrication of functionally graded scaffolds to validate the process monitoring and control strategies described in Chapters 3 and 4. The functional grading is achieved by varying the filament width along the scaffold's reference trajectory. Before fabricating the scaffold, each layer of the reference trajectory is partitioned into repeated sub-tasks, and the reference widths are mapped to the extrusion system input signals using experimentally calibrated models. During fabrication, the profile measurements of the deposited material are collected along each sub-task's trajectory and processed online to determine the material width error. An iterative learning control (ILC) algorithm uses these measurements to learn the inputs for the sub-tasks as they are fabricated, then updates the inputs for the subsequent sub-tasks within the layer.

5.1 Fabrication of Functionally Graded Scaffolds

Scaffolds, a type of 3D periodic structure, have been used in tissue engineering to repair damaged tissues and organs by providing a structure to stimulate tissue regeneration [66]. The porous architecture of a scaffold influences its mechanical and biological functions, both of which must be considered when designing a successful scaffold [67], [68]. As a tissue's role largely dictates its structure, many natural tissues exhibit heterogeneous structures to provide various functions [69]. Hence, functionally graded scaffolds, which are scaffolds with spatially gradient porosities, have been investigated for use in tissue engineering because they can be designed to mimic the function of natural tissues more closely.

Different approaches have been used to vary the porosity in a scaffold spatially. Many designs achieve this simply by changing the spacing between rods [70]–[73]. Alternatively, other designs modify the angle between rods [74] and the rod width [75] in different sections of the layer, or they continuously vary the filament width along the deposition path [25]. As this work aims to control the filament width, a structure with a varying filament width is appealing for validating the process monitoring and control strategies.

5.1.1 Test Scaffold

The structure used to validate the process monitoring and control approach is the functionally graded scaffold shown in Fig. 5.1 based on a similar design from [25]. Each scaffold layer is a rectilinear raster pattern with 24 tapered rods spaced 1.5 mm apart. The height of the first and second layers are 0.25 mm and 0.32 mm, respectively. All rods narrow to a width of 0.65 mm at the midpoint, but the width at the ends of the rod is different due to the differing rod lengths of each layer. In the first layer, the rods are 37.5 mm long and 1 mm wide at the ends; in the second layer, the rods are 34.5 mm long and 0.97 mm wide at the ends. Choosing the lengths as described ensures that the rod midpoints are measured by the process monitoring system. Tapering the rod width along their lengths results in a scaffold with a porosity that increases inward from the corners in the xy-plane.

For the test structure to be suitable for the control strategy described in Chapter 4, the sub-tasks learned by the ILC algorithm, which correspond to the odd-numbered rods, even-numbered rods, and corners of the raster pattern, should have spatially- and iteration-invariant dynamics. When deposited upon a supporting structure (e.g., the substrate or previous layer's material), the filament may be compressed between the support and the nozzle, causing its width to increase or "swell." Thus, the supporting structure for a layer

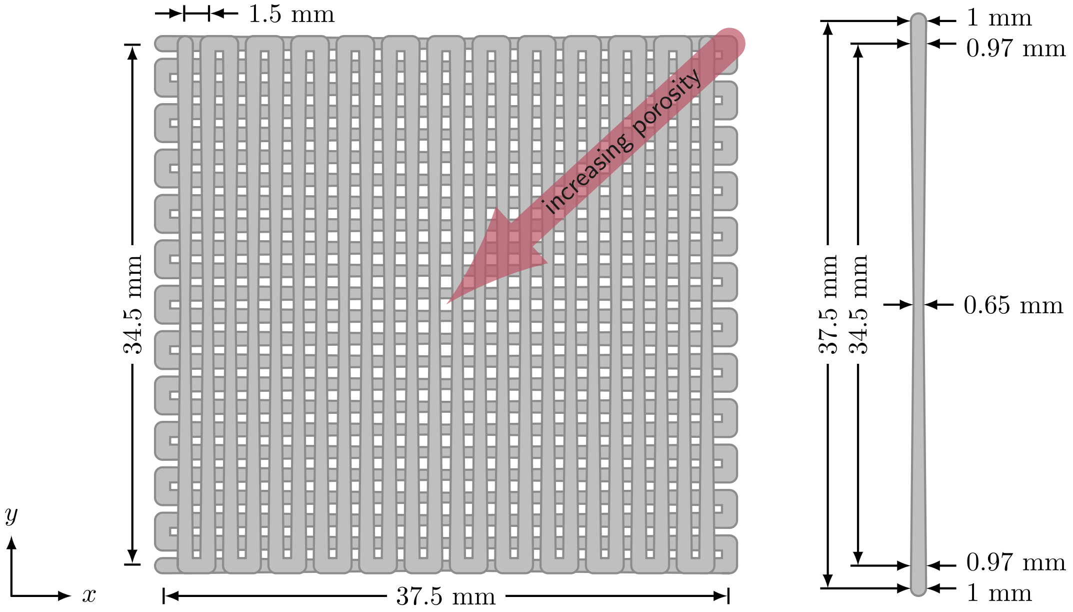

Figure 5.1: The functionally graded scaffold used in experimental validation. Both layers consist of tapered rods with the same tapered filament pattern, shown on the right, that creates a spatially varying porosity in the scaffold. The height of the first and second layers are 0.25 mm and 0.32 mm, respectively.

can be viewed as an external disturbance that acts on the rod width. Unlike the first layer, where the substrate provides a uniform support structure for the entire layer, the second layer is supported non-uniformly by the previous layer's deposited material. If the rods were the same length in both layers, as shown in Fig. 5.2, the second-layer-exterior rods would be the only rods supported by the corners of the first layer; however, the interior rods would be supported by the rods of the first layer. In this case, the different supporting structures would introduce an iteration-varying disturbance into the rod sub-task dynamics that could degrade the performance of the ILC algorithm [29]. Therefore, to avoid introducing an iteration-varying disturbance, we extend the first-layer rods so that their corners are not used to support the second layer.

The support structure also differs between second-layer rods due to the taper of the first-layer filaments. The resulting disturbance repeats at the same frequency since the supporting rods are equally spaced and printed at a constant velocity. However, the taper angle changes the ratio of supported and unsupported material, which can be viewed as varying the duty cycle of the resulting disturbance signal. While the small taper angle will cause a disturbance that varies slightly across iterations, the variation will be minor and should not significantly impact the ILC algorithm's performance.

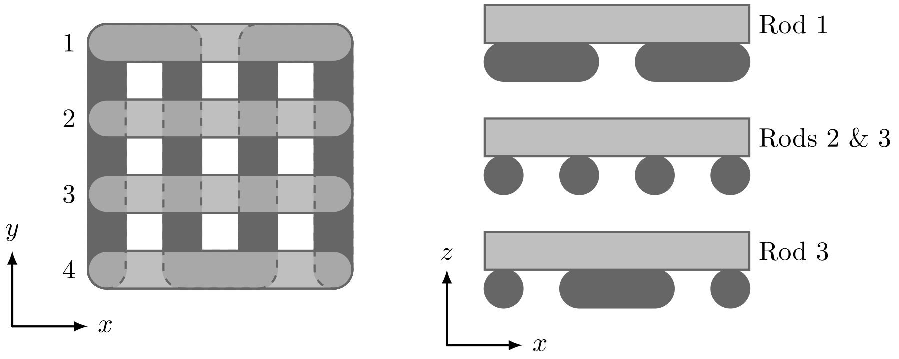

Figure 5.2: The first layer of the scaffold (dark gray) is the supporting structure for the second layer (light gray). The side profiles on the right illustrate the different support structures for the interior and exterior rods. Rod 1 is supported only by corners, rods 2 and 3 are supported only by rods, and rod 4 is supported by both rods and corners.

5.1.2 Printing Parameters

The scaffold structure described in Section 5.1.1 is fabricated at a constant axis velocity of 1 mm/s, and the desired filament width is achieved by varying the extruder torque along the deposition path. The reference filament widths are mapped to the initial extruder torque inputs using the material models identified in Section 4.1. Lead-in lines are added before the start of each layer to initialize the material flow from the extruder. Each layer of the scaffold is printed separately to allow additional data to be collected after fabrication. This data is only used to evaluate performance and not to change the control inputs between layers or prints.

5.1.3 Process Monitoring and Control Implementation

The raster trajectory of the test structure is partitioned into the odd-numbered rod, even-numbered rod, and corner sub-tasks following the segmented ILC approach described in

Section 4.2. These sub-tasks are also the same segments processed online with the algorithm that calculates the material's geometric errors from the scanner measurements (Section 3.4.1). The geometric errors are calculated along the rod sub-tasks using a Gaussian filter with a cut-off wavelength of $\lambda_c = 7$ mm to smooth the measured material edges. Limitations of the process monitoring system result in sparsely measured corner segments, so the geometric errors cannot be calculated effectively for this sub-task. Accordingly, the ILC algorithm (Eq. (4.10)) is applied to correct the measured material width errors in the odd- and even-numbered rod sub-tasks. If error measurements were available along the entire trajectory, the results from implementing ILC in the corner sub-tasks would likely be similar to those for the rod sub-tasks since all sub-tasks use the same ILC update law.

5.2 Printing Results

We fabricate scaffolds described in Section 5.1 using the unmodified inputs generated from the material models and again using the process monitoring and control strategy to update the input signals online; the resulting scaffolds, which we will respectively describe as "uncontrolled" and "controlled," are shown in Fig. 5.3. In the figure, a lead-in line marks the start of each layer's deposition path. Compared with the reference, the entire uncontrolled scaffold appears under-extruded. The initial rods of the controlled print show similar under-extrusion; however, subsequent rods show increased material width as the inputs are learned and updated by the ILC algorithm, especially near the ends of the rods. The increased material width leads to improved pore size in the controlled scaffold compared with the uncontrolled scaffold.

The quality of the fabricated scaffolds is assessed by calculating the material width error at each reference point along the deposition path. Figure 5.4 shows the width error magnitude plotted spatially along the deposition path as a color shading. The colorbar below the figure relates the color shading to the width error magnitude, with darker colors representing

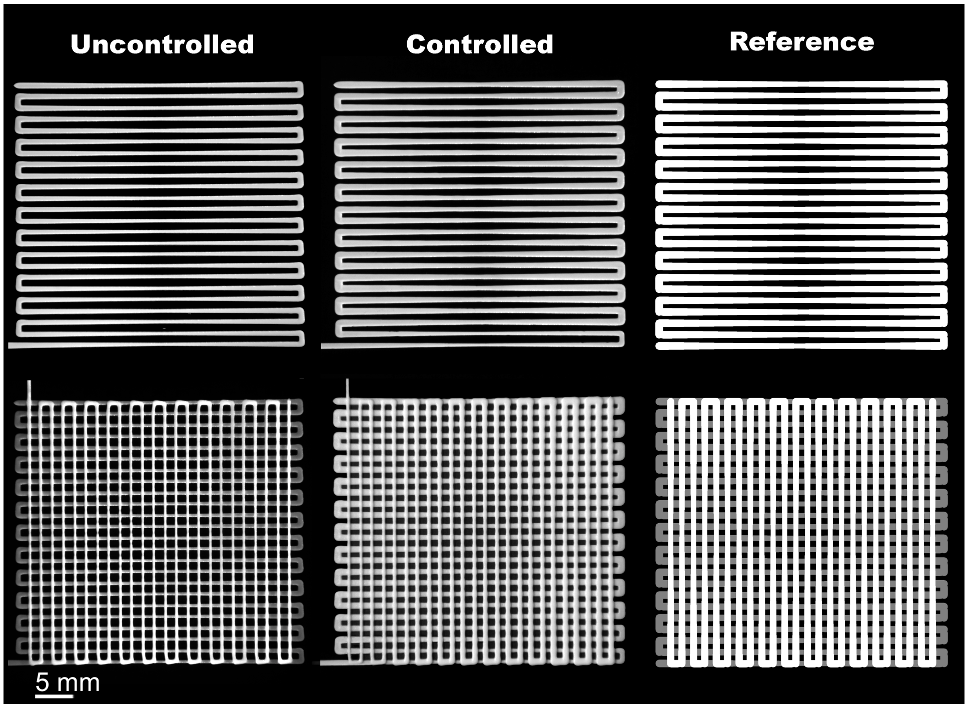

Figure 5.3: Images of the fabricated scaffolds. The top row shows the first layer, while the bottom row shows the second layer. From left to right, the columns show the uncontrolled print, the controlled print, and the reference trajectory. A lead-in line marks the start of each layer.

larger error magnitudes. The black squares in the figure demarcate the start of each layer's deposition path. The uncontrolled prints show similar shading across all rods, signifying that the magnitude of the width error remains consistent throughout both layers of the structure. However, the plots for the controlled prints show a shift from darker to lighter colors after the first rods within a layer, indicating that the width error decreased. This shift aligns with the point when ILC updated the initial input signals.

The error dynamics in the iteration domain further illustrate the impact of the ILC algorithm, as shown in Figs. 5.5 to 5.7. Recall that the odd- and even-numbered rods are the individual sub-tasks learned using ILC. Since a single scaffold layer has 24 rods, each sub-task has twelve total iterations per layer. Although the sub-tasks have separate iteration domains, their iteration domain error dynamics are similar since the odd- and even-numbered rods have the same reference trajectory (Fig. 5.5). Both layers of the controlled print show

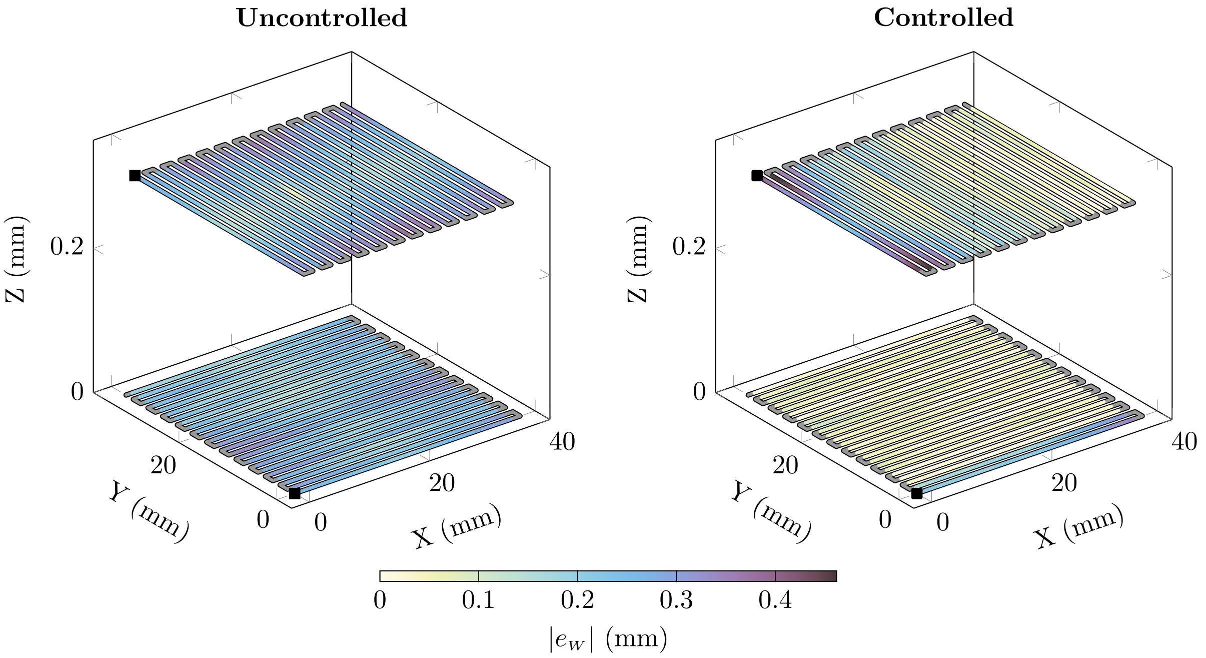

Figure 5.4: The width error magnitude, shown along the reference trajectory as a color shading, for the uncontrolled (left) and controlled (right) prints. Here, lighter colors indicate a smaller error magnitude at a given spatial location. The sections not measured by the process monitoring system, namely the corners of the raster trajectory, are colored gray. A black square indicates the start of each layer's trajectory.

that after iteration 0, the width error magnitude is reduced for all subsequent iterations. In contrast, the uncontrolled layers show no definitive trend in the iteration domain error dynamics (Fig. 5.6).

The reduction to the material width error is additionally quantified using the root mean square (RMS) error. The RMS error is a common metric for evaluating the performance of ILC algorithms and is often normalized at each iteration by the initial iteration's RMS error, i.e., $\mathrm{RMS}(e_j)/\mathrm{RMS}(e_0)$. Plotting the normalized RMS width error in the iteration domain (Fig. 5.7) illustrates the performance difference of the ILC algorithm between the first and second layers of the controlled prints. Specifically, the errors in the controlled print's first layer converge faster than those in the second layer, possibly due to the different support structure in the second layer making the material width less sensitive to input signal changes. The faster error convergence in the first layer contributes to its improved performance over

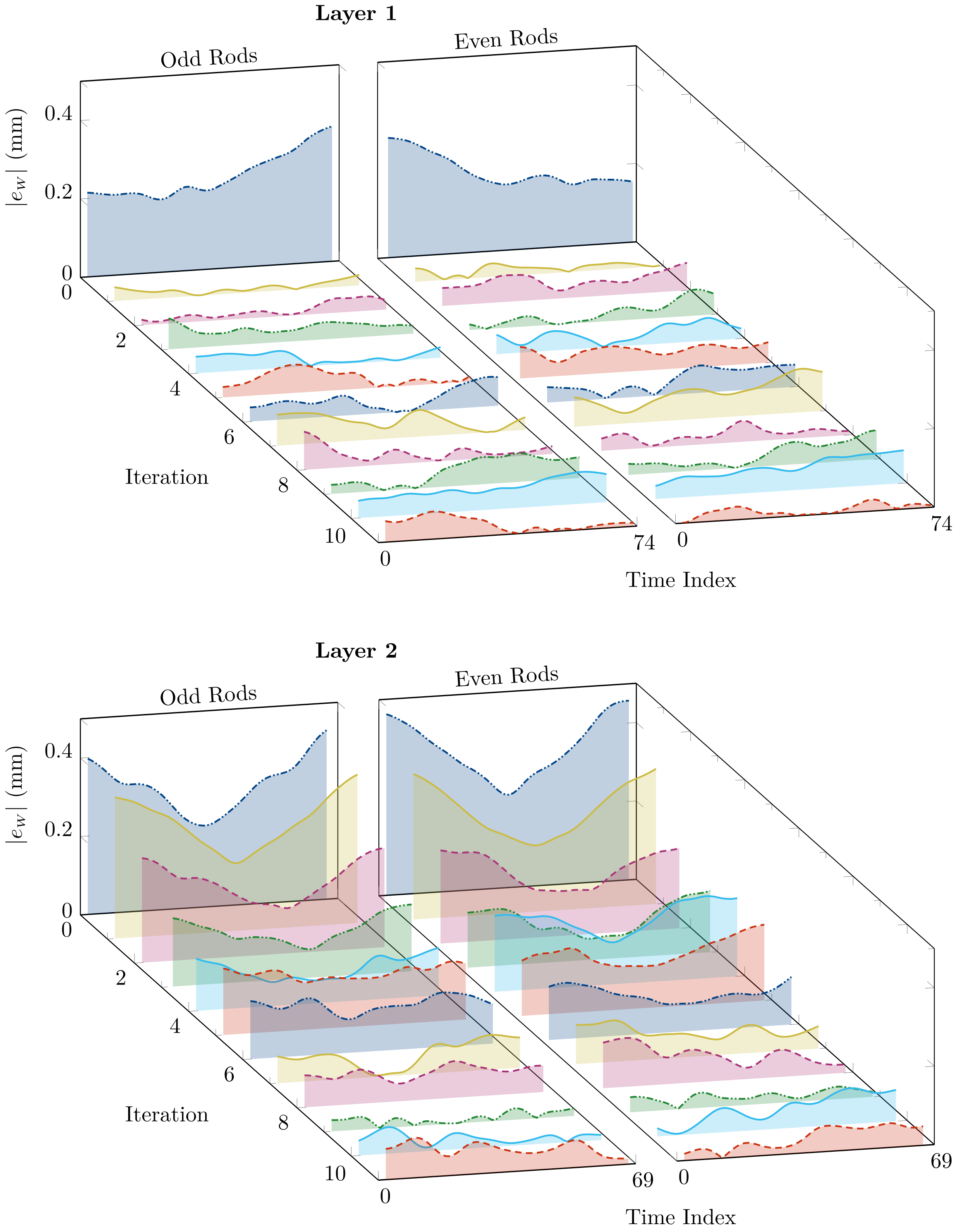

Figure 5.5: Dynamics of the width error magnitude in the iteration and time domains for the sub-tasks in the controlled print. The sub-tasks correspond to the odd- and even-number rods in each layer of the scaffold trajectory.

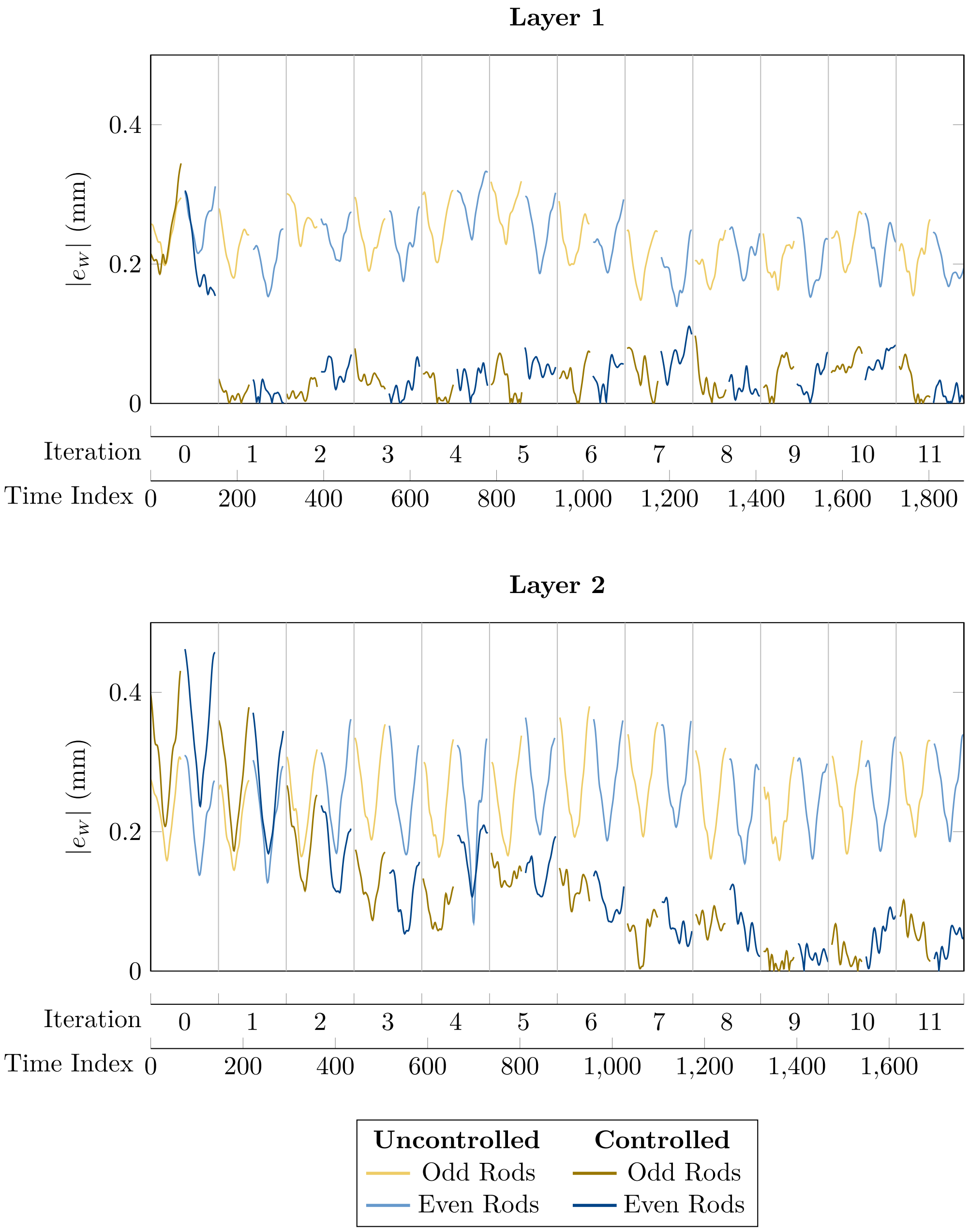

Figure 5.6: Dynamics of the width error magnitude in the iteration and time domains for the uncontrolled and controlled prints.

the second layer. Since the ILC algorithm only modifies the inputs for the rods printed after iteration 0, we compare the RMS error for the initial rods (iteration 0) to the RMS error in the remainder of the print (iterations 1–11). Compared with iteration 0, the RMS error in the rest of the controlled print is reduced by 81.5% and 61.1% in the first and second layers, respectively.

While the error is reduced after the initial rod iterations, the increased errors in the initial sections could impact the performance of the overall structure. One option to reduce the errors in these sections is to add lead-in rods that are used to learn and update the inputs for the initial rods. Furthermore, the initial inputs for subsequent scaffold layers could be learned from previous layers rather than treating the layers as separate tasks. Alternatively, an additional ILC algorithm could be applied part-to-part to learn the inputs from previously fabricated scaffolds.

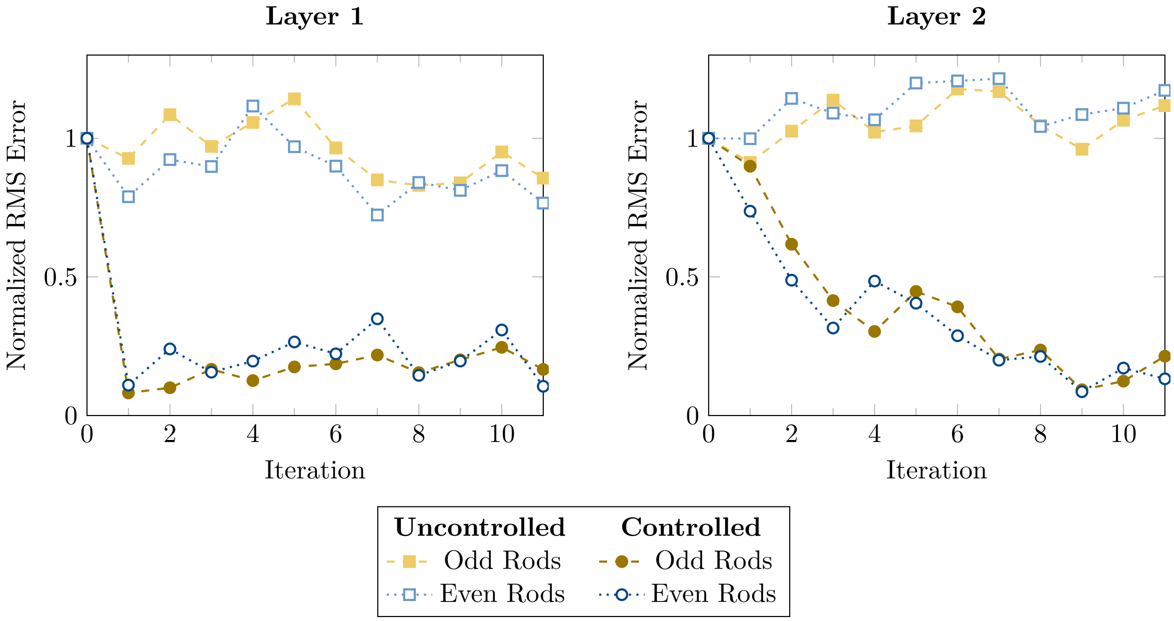

Figure 5.7: Iteration domain RMS width error for the uncontrolled and controlled prints.

Chapter 6

Conclusion

6.1 Summary of Contributions

Additive manufacturing (AM) facilitates the fabrication of complex structures that would otherwise be difficult to make using other manufacturing methods. The spatial and dimensional errors that arise during fabrication using extrusion-based AM methods like direct write (DW) printing inhibit manufacturing parts with increased geometric fidelity. This research presents a method for measuring and correcting geometrical errors in DW-printed 3D periodic structures while they are fabricated. A process monitoring system is developed to measure the deposited material directly, and an iterative learning control (ILC) algorithm is implemented to compensate for the measured errors.

The process monitoring system integrated into the DW printing system utilizes a 2D laser line scanner to take direct *in situ* profile measurements of the deposited material. As the part is fabricated, the laser scanner follows a motion plan that tracks the print head's position, generating time-delayed profile scans of the deposited material. An algorithm is developed to process the scans into a 2D projection of the structure and calculate the material's bead width and centerline contour errors. This algorithm runs during the print, enabling the process monitoring system to determine the part's geometric errors asynchronously, i.e., online but not in real time.

The measurements from the process monitoring system are used to generate models that map the part's reference bead width to the extrusion process's input signals. The ILC algorithm modifies these inputs based on the errors that the process monitoring system measures online. Here, a segmented approach to ILC is taken, where the structure is treated as sets of sub-tasks rather than a single task. For the 3D periodic structures this strategy is applied to, the structure's repeating elements serve as the sub-task sets learned by the ILC algorithm. With this implementation, the learning occurs concurrently with the printing process, which reduces the part's errors as it prints.

6.2 Future Work

While this research demonstrates the ability to measure and correct a fabricated part's geometric errors during the printing process, there are several directions in which future work could improve the current methods. This section presents potential ideas for further increasing part fidelity and expanding the control strategy.

Further improvements to part geometry can be gained by expanding the control approach to correct the material's spatial placement using the centerline contour errors measured by the process monitoring system. One potential strategy to correct contour errors is to modify the axes paths based on a compensation vector formed by mirroring the error about the reference path [13], [76]. Future work could also enable error correction throughout the structure by revising the process monitoring system to reduce the unmeasured sections during a print. Increasing the scanner's sampling rate or shortening the offset between the nozzle and scanner would improve measurement coverage by increasing the measurement density along the material deposition trajectory. Alternatively, augmenting the laser scanner with a camera-based vision system would expand the process monitoring system's field of view. Image processing techniques similar to those used in the current measurement processing algorithm could be utilized to process the output from the camera since the laser scanner's measurements are essentially processed as images. Determining the material's spatial placement, especially distinguishing material on different layers, may be less reliable when using the light intensity captured by the camera instead of the laser scanner's height profiles; however, the camera measurements could be used to estimate the material's placement in the unmeasured sections.

Future work should also investigate methods to decrease the need to post-process prints, which currently involves removing the lead-in lines and likely the uncorrected initial segments of the structure. Incorporating the deposition process' time dynamics into the material models would improve starting and stopping material extrusion, removing the need for lead-in lines. Moreover, the errors in the initial segments could be compensated for by modifying the initial inputs using the ILC algorithm initialized with errors measured from a training routine or previously fabricated parts or layers.

Another direction for future work is to expand the trajectory flexibility of the segmented ILC approach and apply it to fabricate non-periodic structures. One possible strategy, similar to the one explored in [23], would be to create a library of simple parameterized basis elements and then combine different permutations of these elements to form larger, more complex structures. Parameterizing the elements would facilitate designing parts with repeated basis elements to provide trajectory repetition within the structure, allowing a single basis element to be learned with ILC from its various permutations.

References

[1] I. Gibson, D. Rosen, B. Stucker, and M. Khorasani, *Additive Manufacturing Technologies*, Third edition. Cham, Switzerland: Springer, 2021, ISBN: 978-3-030-56127-7. DOI: 10.1007/978-3-030-56127-7.

[2] J. Cesarano, R. Segalman, and P. Calvert, "Robocasting provides moldless fabrication from slurry deposition," *Ceramic Industry*, vol. 148, no. 4, pp. 94–102, Apr. 1998, ISSN: 00090220.

[3] R. P. Chhabra and J. F. Richardson, *Non-Newtonian Flow in the Process Industries: Fundamentals and Engineering Applications*. Butterworth-Heinemann, 1999, ISBN: 0-7506-3770-6.

[4] J. A. Lewis, "Colloidal Processing of Ceramics," *Journal of the American Ceramic Society*, vol. 83, no. 10, pp. 2341–2359, Oct. 2000, ISSN: 00027820, 15512916. DOI: 10.1111/j.1151-2916.2000.tb01560.x.

[5] J. A. Lewis, "Direct Ink Writing of 3D Functional Materials," *Advanced Functional Materials*, vol. 16, no. 17, pp. 2193–2204, Nov. 2006, ISSN: 1616301X, 16163028. DOI: 10.1002/adfm.200600434.

[6] T. D. Ngo, A. Kashani, G. Imbalzano, K. T. Nguyen, and D. Hui, "Additive manufacturing (3D printing): A review of materials, methods, applications and challenges," *Composites Part B: Engineering*, vol. 143, pp. 172–196, Jun. 2018, ISSN: 13598368. DOI: 10.1016/j.compositesb.2018.02.012.

[7] M. Vaezi, H. Seitz, and S. Yang, "A review on 3D micro-additive manufacturing technologies," *The International Journal of Advanced Manufacturing Technology*, vol. 67, no. 5, pp. 1721–1754, Jul. 2013, ISSN: 1433-3015. DOI: 10.1007/s00170-012-4605-2.

[8] R. Landers, U. Hübner, R. Schmelzeisen, and R. Mülhaupt, "Rapid prototyping of scaffolds derived from thermoreversible hydrogels and tailored for applications in tissue engineering," *Biomaterials*, vol. 23, no. 23, pp. 4437–4447, Dec. 2002, ISSN: 01429612. DOI: 10.1016/S0142-9612(02)00139-4.

[9] J. Cesarano, J. G. Dellinger, M. P. Saavedra, *et al.*, "Customization of Load-Bearing Hydroxyapatite Lattice Scaffolds," *International Journal of Applied Ceramic Technology*, vol. 2, no. 3, pp. 212–220, May 2005, ISSN: 1546-542X, 1744-7402. DOI: 10.1111/j.1744-7402.2005.02026.x.

[10] D. Bristow and A. Alleyne, "A manufacturing system for microscale robotic deposition," in *Proceedings of the 2003 American Control Conference, 2003.*, vol. 3, Jun. 2003, 2620–2625 vol.3. DOI: 10.1109/ACC.2003.1243472.

[11] G. M. Gratson, F. García-Santamaría, V. Lousse, *et al.*, "Direct-Write Assembly of Three-Dimensional Photonic Crystals: Conversion of Polymer Scaffolds to Silicon Hollow-Woodpile Structures," *Advanced Materials*, vol. 18, no. 4, pp. 461–465, Feb. 2006, ISSN: 0935-9648, 1521-4095. DOI: 10.1002/adma.200501447.

[12] I. D. Ursan, L. Chiu, and A. Pierce, "Three-dimensional drug printing: A structured review," *Journal of the American Pharmacists Association*, vol. 53, no. 2, pp. 136–144, Mar. 2013, ISSN: 15443191. DOI: 10.1331/JAPhA.2013.12217.

[13] A. A. Armstrong, J. Norato, A. G. Alleyne, and A. J. Wagoner Johnson, "Direct process feedback in extrusion-based 3D bioprinting," *Biofabrication*, vol. 12, no. 1, p. 015 017, Dec. 2019, ISSN: 1758-5090. DOI: 10.1088/1758-5090/ab4d97.

[14] D. Bristow and A. Alleyne, "A High Precision Motion Control System With Application to Microscale Robotic Deposition," *IEEE Transactions on Control Systems Technology*,

vol. 14, no. 6, pp. 1008–1020, Nov. 2006, ISSN: 1558-0865. DOI: 10.1109/TCST.2006.880189.

[15] K. L. Barton and A. G. Alleyne, "A Cross-Coupled Iterative Learning Control Design for Precision Motion Control," *IEEE Transactions on Control Systems Technology*, vol. 16, no. 6, pp. 1218–1231, Nov. 2008, ISSN: 1558-0865. DOI: 10.1109/TCST.2008.919433.

[16] K. L. Barton and A. G. Alleyne, "A Norm Optimal Approach to Time-Varying ILC With Application to a Multi-Axis Robotic Testbed," *IEEE Transactions on Control Systems Technology*, vol. 19, no. 1, pp. 166–180, Jan. 2011, ISSN: 1063-6536, 1558-0865. DOI: 10.1109/TCST.2010.2040476.

[17] X. Chen, W. Zhang, G. Schoenau, and B. Surgenor, "Off-line control of time-pressure dispensing processes for electronics packaging," *IEEE Transactions on Electronics Packaging Manufacturing*, vol. 26, no. 4, pp. 286–293, Oct. 2003, ISSN: 1558-0822. DOI: 10.1109/TEPM.2003.820824.

[18] A. Oleff, B. Küster, M. Stonis, and L. Overmeyer, "Process monitoring for material extrusion additive manufacturing: A state-of-the-art review," *Progress in Additive Manufacturing*, vol. 6, no. 4, pp. 705–730, Dec. 2021, ISSN: 2363-9520. DOI: 10.1007/s40964-021-00192-4.

[19] S. A. Tofail, E. P. Koumoulos, A. Bandyopadhyay, S. Bose, L. O'Donoghue, and C. Charitidis, "Additive manufacturing: Scientific and technological challenges, market uptake and opportunities," *Materials Today*, vol. 21, no. 1, pp. 22–37, Jan. 2018, ISSN: 13697021. DOI: 10.1016/j.mattod.2017.07.001.

[20] B. Yao, F. Imani, and H. Yang, "Markov Decision Process for Image-Guided Additive Manufacturing," *IEEE Robotics and Automation Letters*, vol. 3, no. 4, pp. 2792–2798, Oct. 2018, ISSN: 2377-3766, 2377-3774. DOI: 10.1109/LRA.2018.2839973.

[21] D. J. Hoelzle, A. G. Alleyne, and A. J. Wagoner Johnson, "Iterative Learning Control for robotic deposition using machine vision," in *2008 American Control Conference*,

Seattle, WA, USA, Jun. 2008, pp. 4541–4547, ISBN: 978-1-4244-2078-0. DOI: 10.1109/ACC.2008.4587211.

[22] D. J. Hoelzle, A. G. Alleyne, and A. J. Wagoner Johnson, “Iterative Learning Control using a basis signal library,” in *2009 American Control Conference*, St. Louis, MO, USA: IEEE, 2009, pp. 925–930, ISBN: 978-1-4244-4523-3. DOI: 10.1109/ACC.2009.5160565.

[23] D. J. Hoelzle, A. G. Alleyne, and A. J. Wagoner Johnson, “Basis Task Approach to Iterative Learning Control With Applications to Micro-Robotic Deposition,” *IEEE Transactions on Control Systems Technology*, vol. 19, no. 5, pp. 1138–1148, Sep. 2011, ISSN: 1558-0865. DOI: 10.1109/TCST.2010.2063030.

[24] A. A. Armstrong, A. G. Alleyne, and A. J. Wagoner Johnson, “1D and 2D error assessment and correction for extrusion-based bioprinting using process sensing and control strategies,” *Biofabrication*, vol. 12, no. 4, p. 045 023, Aug. 2020, ISSN: 1758-5082. DOI: 10.1088/1758-5090/aba8ee.

[25] A. A. Armstrong, A. Pfeil, A. G. Alleyne, and A. J. Wagoner Johnson, “Process monitoring and control strategies in extrusion-based bioprinting to fabricate spatially graded structures,” *Bioprinting*, vol. 21, e00126, Mar. 2021, ISSN: 2405-8866. DOI: 10.1016/j.bprint.2020.e00126.

[26] A. A. Armstrong and A. G. Alleyne, “A Multi-Input Single-Output iterative learning control for improved material placement in extrusion-based additive manufacturing,” *Control Engineering Practice*, vol. 111, p. 104 783, Jun. 2021, ISSN: 09670661. DOI: 10.1016/j.conengprac.2021.104783.

[27] M. Piovarci, M. Foshey, J. Xu, *et al.*, “Closed-Loop Control of Direct Ink Writing via Reinforcement Learning,” *ACM Transactions on Graphics*, vol. 41, no. 4, 112:1–112:10, Jul. 2022, ISSN: 0730-0301. DOI: 10.1145/3528223.3530144. arXiv: 2201.11819 [cs].

[28] S. Arimoto, S. Kawamura, and F. Miyazaki, “Bettering operation of Robots by learning,” *Journal of Robotic Systems*, vol. 1, no. 2, pp. 123–140, 1984, ISSN: 07412223, 10974563. DOI: `10.1002/rob.4620010203`.

[29] D. Bristow, M. Tharayil, and A. Alleyne, “A survey of iterative learning control,” *IEEE Control Systems Magazine*, vol. 26, no. 3, pp. 96–114, Jun. 2006, ISSN: 1941-000X. DOI: `10.1109/MCS.2006.1636313`.

[30] R. Horowitz, “Learning Control of Robot Manipulators,” *Journal of Dynamic Systems, Measurement, and Control*, vol. 115, no. 2B, pp. 402–411, Jun. 1993, ISSN: 0022-0434. DOI: `10.1115/1.2899080`.

[31] D. A. Bristow, “Iterative Learning Control for Precision Motion Control of Microscale and Nanoscale Tracking Systems,” Ph.D. dissertation, University of Illinois at Urbana-Champaign, 2007.

[32] A. Armstrong, “Direct Process Feedback in Extrusion-Based Additive Manufacturing Using an Improved Iterative Learning Control Approach,” Ph.D. dissertation, University of Illinois at Urbana-Champaign, Dec. 2020.

[33] S. S. Igram, “A Distributed Hierarchical Iterative Learning Control Framework,” Ph.D. dissertation, University of Illinois at Urbana-Champaign, Jul. 2022.

[34] J. Bolder, T. Oomen, S. Koekebakker, and M. Steinbuch, “Using iterative learning control with basis functions to compensate medium deformation in a wide-format inkjet printer,” *Mechatronics*, vol. 24, no. 8, pp. 944–953, Dec. 2014, ISSN: 0957-4158. DOI: `10.1016/j.mechatronics.2014.07.003`.

[35] J. Bolder, T. Oomen, and M. Steinbuch, “On inferential Iterative Learning Control: With example to a printing system,” in *2014 American Control Conference*, Jun. 2014, pp. 1827–1832. DOI: `10.1109/ACC.2014.6858946`.

[36] Z. Xiong and J. Zhang, "Product Quality Trajectory Tracking in Batch Processes Using Iterative Learning Control Based on Time-Varying Perturbation Models," *Industrial & Engineering Chemistry Research*, vol. 42, no. 26, pp. 6802–6814, Dec. 2003, ISSN: 0888-5885. DOI: 10.1021/ie034006j.

[37] L. Tang and R. G. Landers, "Melt Pool Temperature Control for Laser Metal Deposition Processes—Part II: Layer-to-Layer Temperature Control," *Journal of Manufacturing Science and Engineering*, vol. 132, no. 1, Jan. 2010, ISSN: 1087-1357, 1528-8935. DOI: 10.1115/1.4000883.

[38] P. M. Sammons, D. A. Bristow, and R. G. Landers, "Iterative learning control of bead morphology in Laser Metal Deposition processes," in *2013 American Control Conference*, Jun. 2013, pp. 5942–5947. DOI: 10.1109/ACC.2013.6580770.

[39] A. Heralić, A.-K. Christiansson, and B. Lennartson, "Height control of laser metal-wire deposition based on iterative learning control and 3D scanning," *Optics and Lasers in Engineering*, vol. 50, no. 9, pp. 1230–1241, Sep. 2012, ISSN: 0143-8166. DOI: 10.1016/j.optlaseng.2012.03.016.

[40] L. Tang and R. G. Landers, "Layer-to-Layer Height Control for Laser Metal Deposition Process," *Journal of Manufacturing Science and Engineering*, vol. 133, no. 2, Mar. 2011, ISSN: 1087-1357, 1528-8935. DOI: 10.1115/1.4003691.

[41] P. Hagqvist, A. Heralić, A.-K. Christiansson, and B. Lennartson, "Resistance based iterative learning control of additive manufacturing with wire," *Mechatronics*, vol. 31, pp. 116–123, Oct. 2015, ISSN: 0957-4158. DOI: 10.1016/j.mechatronics.2015.03.008.

[42] M. J. Spector, Y. Guo, S. Roy, M. O. Bloomfield, A. Maniatty, and S. Mishra, "Passivity-based Iterative Learning Control Design for Selective Laser Melting," in *2018 Annual American Control Conference (ACC)*, Jun. 2018, pp. 5618–5625. DOI: 10.23919/ACC.2018.8431782.

[43] A. Nettekoven, S. Fish, U. Topcu, and J. Beaman, “Predictive Iterative Learning Control with Data-Driven Model for Optimal Laser Power in Selective Laser Sintering,” University of Texas at Austin, 2018. DOI: `10.26153/tsw/17226`.

[44] A. Shkoruta, W. Caynoski, S. Mishra, and S. Rock, “Iterative learning control for power profile shaping in selective laser melting,” in *2019 IEEE 15th International Conference on Automation Science and Engineering (CASE)*, Aug. 2019, pp. 655–660. DOI: `10.1109/COASE.2019.8843070`.

[45] L. Funke and M. Opara, “Using Iterative Learning Control to Improve the Accuracy of Desktop Fused Deposition Modeling Printers: An Experimental Case Study,” in *ASME 2022 17th International Manufacturing Science and Engineering Conference*, American Society of Mechanical Engineers Digital Collection, Sep. 2022. DOI: `10.1115/MSEC2022-78324`.

[46] D. J. Hoelzle and K. L. Barton, “On Spatial Iterative Learning Control via 2-D Convolution: Stability Analysis and Computational Efficiency,” *IEEE Transactions on Control Systems Technology*, vol. 24, no. 4, pp. 1504–1512, Jul. 2016, ISSN: 1558-0865. DOI: `10.1109/TCST.2015.2501344`.

[47] Z. Wang, C. P. Pannier, K. Barton, and D. J. Hoelzle, “Application of robust monotonically convergent spatial iterative learning control to microscale additive manufacturing,” *Mechatronics*, vol. 56, pp. 157–165, Dec. 2018, ISSN: 0957-4158. DOI: `10.1016/j.mechatronics.2018.09.003`.

[48] L. Aarnoudse, C. Pannier, Z. Afkhami, T. Oomen, and K. Barton, “Multi-Layer Spatial Iterative Learning Control for Micro-Additive Manufacturing,” *IFAC-PapersOnLine*, vol. 52, no. 15, pp. 97–102, 2019, ISSN: 24058963. DOI: `10.1016/j.ifacol.2019.11.657`.

[49] Z. Afkhami, C. Pannier, L. Aarnoudse, D. Hoelzle, and K. Barton, “Spatial Iterative Learning Control for Multi-material Three-Dimensional Structures,” *ASME Letters*

in Dynamic Systems and Control, vol. 1, no. 1, Mar. 2020, ISSN: 2689-6117. DOI: 10.1115/1.4046576.

[50] N. Paxton, W. Smolan, T. Böck, F. Melchels, J. Groll, and T. Jungst, "Proposal to assess printability of bioinks for extrusion-based bioprinting and evaluation of rheological properties governing bioprintability," *Biofabrication*, vol. 9, no. 4, p. 044 107, Nov. 2017, ISSN: 1758-5090. DOI: 10.1088/1758-5090/aa8dd8.

[51] P. S. Gungor-Ozkerim, I. Inci, Y. Shrike Zhang, A. Khademhosseini, and M. Remzi Dokmeci, "Bioinks for 3D bioprinting: An overview," *Biomaterials Science*, vol. 6, no. 5, pp. 915–946, 2018. DOI: 10.1039/C7BM00765E.

[52] M. Hospodiuk, M. Dey, D. Sosnoski, and I. T. Ozbolat, "The bioink: A comprehensive review on bioprintable materials," *Biotechnology Advances*, vol. 35, no. 2, pp. 217–239, Mar. 2017, ISSN: 07349750. DOI: 10.1016/j.biotechadv.2016.12.006.

[53] S. Kyle, Z. M. Jessop, A. Al-Sabah, and I. S. Whitaker, "'Printability' of Candidate Biomaterials for Extrusion Based 3D Printing: State-of-the-Art," *Advanced Healthcare Materials*, vol. 6, no. 16, p. 1 700 264, Aug. 2017, ISSN: 21922640. DOI: 10.1002/adhm.201700264.

[54] T. Jiang, J. G. Munguia-Lopez, S. Flores-Torres, J. Kort-Mascort, and J. M. Kinsella, "Extrusion bioprinting of soft materials: An emerging technique for biological model fabrication," *Applied Physics Reviews*, vol. 6, no. 1, p. 011 310, Mar. 2019. DOI: 10.1063/1.5059393.

[55] M. W. Spong, S. Hutchinson, and M. Vidyasagar, *Robot Modeling and Control*. Hoboken, NJ : John Wiley & Sons, 2006, ISBN: 0-471-64990-2.

[56] B. Siciliano, L. Sciavicco, L. Villani, and G. Oriolo, *Robotics: Modelling, Planning and Control*. London, United Kingdom: Springer London, Limited, 2009, ISBN: 978-1-84628-642-1.

[57] G. Bradski, “The OpenCV library,” *Dr. Dobb’s Journal*, vol. 25, no. 11, pp. 120–125, Nov. 2000, ISSN: 1044789X.

[58] N. Otsu, “A Threshold Selection Method from Gray-Level Histograms,” *IEEE Transactions on Systems, Man, and Cybernetics*, vol. 9, no. 1, pp. 62–66, Jan. 1979, ISSN: 2168-2909. DOI: 10.1109/TSMC.1979.4310076.

[59] X. Xu, S. Xu, L. Jin, and E. Song, “Characteristic analysis of Otsu threshold and its applications,” *Pattern Recognition Letters*, vol. 32, no. 7, pp. 956–961, May 2011, ISSN: 0167-8655. DOI: 10.1016/j.patrec.2011.01.021.

[60] R. O. Duda and P. E. Hart, *Pattern Classification and Scene Analysis*. New York: Wiley, 1973, ISBN: 978-0-471-22361-0.

[61] A. Rosenfeld and J. L. Pfaltz, “Distance functions on digital pictures,” *Pattern Recognition*, vol. 1, no. 1, pp. 33–61, Jul. 1968, ISSN: 0031-3203. DOI: 10.1016/0031-3203(68)90013-7.

[62] G. Borgefors, “Distance transformations in digital images,” *Computer Vision, Graphics, and Image Processing*, vol. 34, no. 3, pp. 344–371, Jun. 1986, ISSN: 0734-189X. DOI: 10.1016/S0734-189X(86)80047-0.

[63] A. Simeunović and D. J. Hoelzle, “Nonlinear and linearized gray box models of direct-write printing dynamics,” *Rapid Prototyping Journal*, vol. 26, no. 10, pp. 1665–1676, Jan. 2020, ISSN: 1355-2546. DOI: 10.1108/RPJ-12-2018-0303.

[64] X. B. Chen, “Modeling of rotary screw fluid dispensing processes,” *Journal of Electronic Packaging, Transactions of the ASME*, vol. 129, no. 2, 2007, ISSN: 10437398. DOI: 10.1115/1.2721090.

[65] R. Suntornnond, E. Y. S. Tan, J. An, and C. K. Chua, “A Mathematical Model on the Resolution of Extrusion Bioprinting for the Development of New Bioinks,” *Materials*, vol. 9, no. 9, p. 756, Sep. 2016, ISSN: 1996-1944. DOI: 10.3390/ma9090756.

[66] D. W. Hutmacher, "Scaffolds in Tissue Engineering Bone and Cartilage," p. 15, 2000, ISSN: 0142-9612 , 1878-5905. DOI: 10.1016/S0142-9612(00)00121-6.

[67] A. K. M. Khoda, I. T. Ozbolat, and B. Koc, "A functionally gradient variational porosity architecture for hollowed scaffolds fabrication," *Biofabrication*, vol. 3, no. 3, p. 034 106, Jul. 2011, ISSN: 1758-5090. DOI: 10.1088/1758-5082/3/3/034106.

[68] A. K. M. B. Khoda and B. Koc, "Functionally heterogeneous porous scaffold design for tissue engineering," *Computer-Aided Design*, vol. 45, no. 11, pp. 1276–1293, Nov. 2013, ISSN: 0010-4485. DOI: 10.1016/j.cad.2013.05.005.

[69] K. F. Leong, C. K. Chua, N. Sudarmadji, and W. Y. Yeong, "Engineering functionally graded tissue engineering scaffolds," *Journal of the Mechanical Behavior of Biomedical Materials*, vol. 1, no. 2, pp. 140–152, Apr. 2008, ISSN: 1751-6161. DOI: 10.1016/j.jmbbm.2007.11.002.

[70] T. Woodfield, C. V. Blitterswijk, J. D. Wijn, T. Sims, A. Hollander, and J. Riesle, "Polymer Scaffolds Fabricated with Pore-Size Gradients as a Model for Studying the Zonal Organization within Tissue-Engineered Cartilage Constructs," *Tissue Engineering*, vol. 11, no. 9-10, pp. 1297–1311, Sep. 2005, ISSN: 1076-3279. DOI: 10.1089/ten.2005.11.1297.

[71] A. K. M. B. Khoda, I. T. Ozbolat, and B. Koc, "Engineered Tissue Scaffolds With Variational Porous Architecture," *Journal of Biomechanical Engineering*, vol. 133, no. 1, Dec. 2010, ISSN: 0148-0731. DOI: 10.1115/1.4002933.

[72] J. M. Sobral, S. G. Caridade, R. A. Sousa, J. F. Mano, and R. L. Reis, "Three-dimensional plotted scaffolds with controlled pore size gradients: Effect of scaffold geometry on mechanical performance and cell seeding efficiency," *Acta Biomaterialia*, vol. 7, no. 3, pp. 1009–1018, Mar. 2011, ISSN: 1742-7061. DOI: 10.1016/j.actbio.2010.11.003.

[73] A. D. Luca, A. Longoni, G. Criscenti, C. Mota, C. van Blitterswijk, and L. Moroni, "Toward mimicking the bone structure: Design of novel hierarchical scaffolds with a tailored radial porosity gradient," *Biofabrication*, vol. 8, no. 4, p. 045 007, Oct. 2016, ISSN: 1758-5090. DOI: 10.1088/1758-5090/8/4/045007.

[74] I. Zein, D. W. Hutmacher, K. C. Tan, and S. H. Teoh, "Fused deposition modeling of novel scaffold architectures for tissue engineering applications," *Biomaterials*, vol. 23, no. 4, pp. 1169–1185, Feb. 2002, ISSN: 0142-9612. DOI: 10.1016/S0142-9612(01)00232-0.

[75] S. J. Kalita, S. Bose, H. L. Hosick, and A. Bandyopadhyay, "Development of controlled porosity polymer-ceramic composite scaffolds via fused deposition modeling," *Materials Science and Engineering: C*, vol. 23, no. 5, pp. 611–620, Oct. 2003, ISSN: 0928-4931. DOI: 10.1016/S0928-4931(03)00052-3.

[76] H. T. Bandy, M. A. Donmez, D. E. Gilsinn, *et al.*, "A Methodology for Compensating Errors Detected by Process-Intermittent Inspection," NIST, Tech. Rep. 6811, Oct. 2001, pp. 1–77.

Appendix A

The Gaussian Filter

In the continuous domain, the impulse response for a Gaussian filter is defined as

$$g(x) = \frac{1}{\sigma\sqrt{2\pi}} \exp\left(-\frac{x^2}{2\sigma^2}\right). \tag{A.1}$$

Performing the Fourier transform on Eq. (A.1) yields the filter's frequency response, given as

$$G(j\omega) = \exp\left(-\frac{\omega^2\sigma^2}{2}\right) \tag{A.2}$$

where the parameter σ can be used to tune the filter's frequency response. The filter parameter σ can be defined in terms of the cut-off frequency ω_c, which is the frequency at which the filter's frequency response is $|G(j\omega_c)| = -3$ dB. However, because the Gaussian filters are applied spatially in this application, it is more intuitive to define the cut-off in terms of the spatial wavelength λ, which is related to the frequency by $\omega = 2\pi/\lambda$. Solving for the wavelength at which $|G(j2\pi/\lambda)| = -3$ dB yields the following relationship between the cut-off wavelength λ_c and σ:

$$\sigma = \lambda_c \frac{\sqrt{\ln 2}}{2\pi}. \tag{A.3}$$

Since the Gaussian filter is applied to a set of discrete points rather than a continuous profile, the filter is implemented in the discrete domain using the sampled impulse response, given as

$$g_d(k) = \frac{1}{\sigma\sqrt{2\pi}} \exp\left(-\frac{k^2 d_s^2}{2\sigma^2}\right), \quad \text{for } -m \leq k \leq m \tag{A.4}$$

where d_s is the distance between sampled points and the parameter m defines the span of the filter. It should be noted that Eq. (A.4) assumes the distance between points d_s is constant. While the distance between points in the edge profiles to which the filter is applied will vary slightly, it is reasonable to assume a constant distance d_s between edge points based on the simulation results shown in Fig. 3.7. Thus, we assume the distance between points is equal to $d_s = v/f_s$, where v is the axis velocity and f_s is the sampling rate of the scanner. Additionally, the selected cutoff wavelength is assumed to be larger than the Nyquist wavelength, which is the shortest resolvable wavelength and given as twice the sampling distance.

Although the filter's impulse response extends infinitely, it can be approximated as a finite impulse response (FIR) filter. Since the values of the sampled impulse response decay as m increases, the contributions to the filtered output from the points outside of the truncated span will be negligible if the filter's span is sufficiently long. Therefore, we truncate the filter by finding the integer m that satisfies

$$g_d(m) \leq \varepsilon g_d(0) \tag{A.5}$$

where ε is an arbitrarily small value. Solving Eq. (A.5) for m yields that

$$m \geq \frac{\sigma}{d_s}\sqrt{-2\ln\varepsilon}. \tag{A.6}$$

When truncating the impulse response, we use $\varepsilon = 10^{-3}$ and choose m as the nearest integer greater than Eq. (A.6). Sampling and truncating the impulse response can alter the filter's DC gain so the sampled filter is normalized to ensure a unitary DC gain, i.e.,

$$\bar{g}_d(k) = \frac{g_d(k)}{\sum_{l=-m}^{m} g_d(l)}. \tag{A.7}$$

The filter is applied as a discrete convolution with the sampled impulse response. Given a discrete profile $y(k)$, $k \in [0, N-1]$, the filtered output $z(k)$ is

$$z(k) = \sum_{i=-m}^{m} \bar{g}_d(i) y(k+i), \quad \text{for } k \in [m, N-1-m]. \tag{A.8}$$

Note that Eq. (A.8) only determines the filtered output for $k \in [m, N-1-m]$ because, outside this interval, the term $y(k+i)$ is not defined for all values of $i \in [-m, m]$. To filter the ends of the profile, we adjust the weights of the Gaussian filter based on the sample index to maintain a unitary DC gain. Therefore, the filtered output over the entire profile interval is

$$z(k) = \sum_{i=a}^{b} \frac{\bar{g}_d(i)}{S} y(k+i), \quad \text{with } S = \sum_{l=a}^{b} \bar{g}_d(l), \quad \text{for } k \in [0, N-1] \tag{A.9}$$

where the bounds are

$$\begin{aligned} a &= -\min(m, k) \\ b &= \min(m, N-1-k). \end{aligned} \tag{A.10}$$